Fall 12-18-2015

Submarine Channel Evolution Linked to Rising Salt Dome, Mississippi Canyon, Gulf of Mexico

Rachel C. Carter
University of New Orleans, rcarter4@uno.edu

Submarine Channel Evolution Linked to Rising Salt Dome, Mississippi Canyon, Gulf of Mexico

A Thesis

Submitted to the Graduate Faculty of the
University of New Orleans
in partial fulfillment of
the requirements for the degree of

Master of Science
In
Earth and Environmental Sciences

By

Rachel Carter

B.S. University of New Orleans, 2013

December, 2015

Acknowledgment

I thank Western Geco for donating the 3D seismic dataset used in this study. A special thanks to IHS for donating licenses of Kingdom and the Rock Solid Attributes add-on to the University of New Orleans. Thanks are also due to the New Orleans Geological Society, who helped donate HP workstations to the Department, and who continuously mentor students and support students' passion for science. I would also like to acknowledge my advisors, who have patiently bestowed their knowledge upon me, and will never know how much they are appreciated. I would like to dedicate this work to my loving and supportive family.

Table of Contents

List of Figures

List of Tables

Nomenclature and Abbreviations

Mississippi Canyon ..... MC
Gulf of Mexico ..... GOM
Three Dimensional 3D

Abstract

By examining halokinetics and channel evolution in a deep-water system, we investigate how submarine channel morphology is affected by changing seascape linked to diapirism. The study area is located in Mississippi Canyon, Gulf of Mexico (GOM), situated directly off the continental slope in a prominent salt dome region. Interactions of salt domes with submarine channels in the GOM are poorly documented. Utilizing 3D seismic data and seismic geomorphology techniques, a long-lived Plio-Pleistocene submarine channel system has been investigated to develop a relationship between variable phases of salt movement and plan-form morphology of preserved channels.

We suggest that halokinetics acts as a driver for topographic-channel evolution in the study area. We show how submarine channel morphology can be directly controlled by halokinetics, where salt movement can act as a structural control on both location and morphology of meandering channel complexes. Channels are able to move towards an equilibrium state only when holokinetics decreases.

Keywords: Mississippi Canyon, Gulf of Mexico; halokinetics; meandering submarine channels; sinuosity; seismic geomorphology; seismic attributes

Introduction

Submarine channels have a dynamic relationship with seafloor topography (Gamboa et al., 2012; Posamentier et al., 2003; Deb et al., 2012). Channels are extremely sensitive to even minor changes of both slope and sediment load (Gee et al., 2007; Damuth et al., 1988). This sensitivity can be seen not only in erosive power, but also in the overall location and morphology of the channel. For example, channels adjust by migrating towards structural lows, and increase in channel slope can lead to a decrease in meander intensity (Schumm et al., 1972). Thus changes in topography can directly influence channel morphology.

While there is a plethora of studies on Neogene submarine channels in the Gulf of Mexico (GOM) (Galloway et al., 2000; Nelson et al., 2010; Snedden et al., 2012), their interactions with salt domes are remarkably poorly documented. Previous studies on the interaction of salt movement and channel evolution in other places used mostly traditional methods of channel visualization. Gee et al. (2006) examined drill and core data along with amplitudes and geometry of 3D seismic data to investigate the control of salt domes on channel styles, geometries and facies in offshore Angola. Loncke et al. (2006) illustrated the interaction of sediment, salt tectonics and paleotopographic features in the Nile deep-sea fan based on multi-channel seismic and gravity data. Gamboa et al. (2012) used statistical analysis techniques to correlate geometries of channel confluence with topographic confinement created by salt domes in the Espírito Santo Basin, Brazil. While these studies are extensive, they leave lingering questions about the effects that salt diapirism rates and associated accommodation space have on the stability, sinuosity and overall morphology of submarine channels.

Submarine channels are often difficult to identify and interpret properly due to poor visualization, quality of resolution, and pitfalls of time slice interpretation. A better understanding of channel interaction with changing topography is clearly needed. This study aims to reduce these pitfalls by using high-resolution 3D seismic data with vertical limits of detection as low as ~7 m, performing multiple attribute analyses, and by employing horizons slices of coeval surfaces instead of time slices.

This study utilizes 3D seismic data along with wireline log and biostratigraphic data. With the help of seismic geomorphology techniques and cutting-edge channel visualization methods, this study investigates the interactions between channel evolution and changing seascape driven by halokinetics for a meandering Plio-Plistocene submarine channel complex.

Geologic Setting

The GOM is a syn-exhumation salt basin (Rowan, 2014). The study area is in the northern region of Mississippi Canyon, GOM, and is situated directly off the continental slope at a water depth of 1,645 m [5400ft] (Milkov et al., 2007) in a prominent salt dome region (Fig. 1). The field is an immature primary basin within the disconnected salt-stock-canopy province (Pilcher et al., 2011) (Fig. 2).

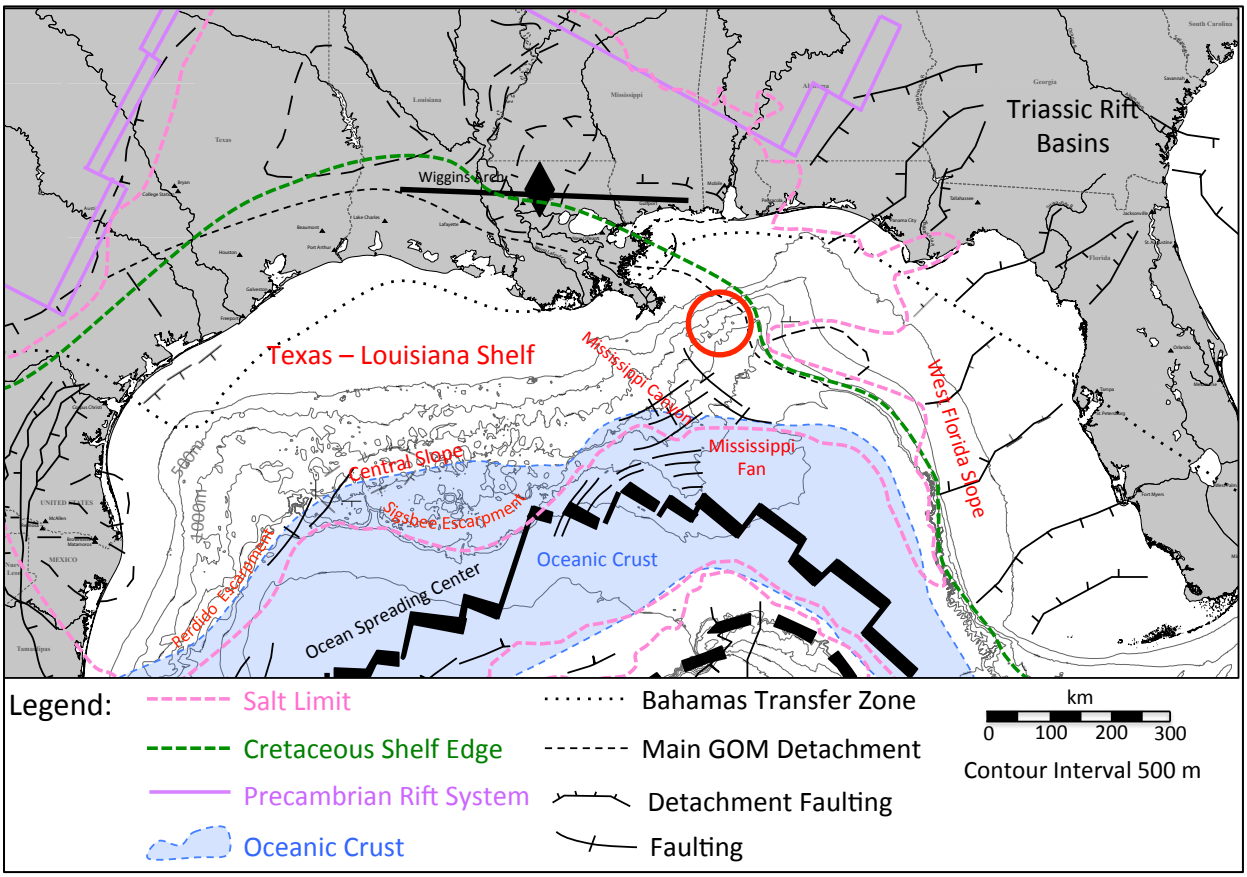

Figure 1. Regional view of the Northern GOM basin. Predominant features and major tectonic features are labeled. Bathymetric contour lines, with a contour interval of 500 m, show the continental shelf and slope as well as the effect of diapiring salt on sea floor topography. The structural evolution of the GOM has been controlled by the flow of the Louann Salt and its excavation into near-surface diapirs and sheets. Arial extent of 3D seismic data utilized in this study occurs within red circle. (Image modified from: Pindell et al., 2009; NOAA website (http://www.ngdc.noaa.gov/mgg last access: 9/17/2015)

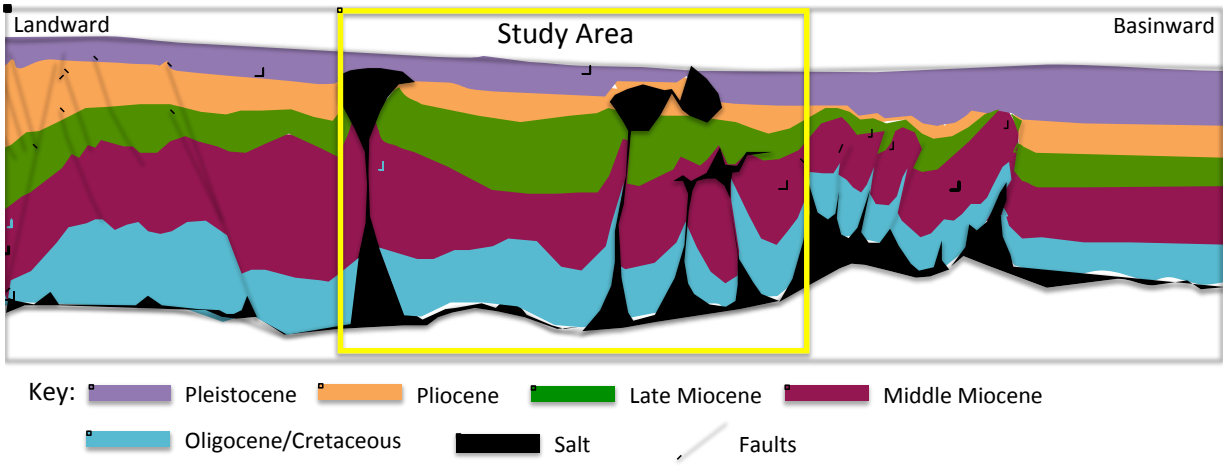

Figure 2. The image is a generalized cross section through the disconnected salt-stock-canopy province of Mississippi Canyon. The study area is an immature primary basin within this province and is located within the yellow box. (Modified from Pilcher et al., 2011).

Early-Mid Jurassic rifting instigated stretching and thinning of the continental crust that opened up a small connection with the Atlantic Ocean, allowing the GOM to become a restricted basin with suitable conditions for deposition of the Louann Salt (Konyukhov, 2008). The Louann salt was a vast deposit with an average thickness of 1,525 m [5,000 ft.] (Mondelli, 2011). Variable thicknesses of the Louann salt were due in part to larger concentrations of salt within paleo-graben structures (Mancini, 1991; Wu et al., 1990) that has since affected the entire structure of the GOM Basin. During the Late Jurassic (Oxfordian), oceanic crust began to form. Subsequent rifting of the basin occurred as the Yucatan block moved away from North America (Rowan, 2014), prompting the opening of the GOM, which allowed for adequate ocean water circulation. The Louann Salt ceased to deposit as a result of this basin opening. The structural evolution of the Northern GOM can be linked to the irregular deposition of the Louann Salt. The sea floor topography of the GOM has been controlled by the flow of the Louann Salt and its re-mobilization into near-surface diapirs and sheets (Rowan et al., 1998).

The Cenozoic brought immense amounts of sediment deposition in the Northern GOM. Large fluvio-deltaic systems formed in the late Paleocene due to large volumes of clastic sediment being transported from inland into the basin (Galloway, 2008). However, our study area lacked major fluvial input and limited deposition during the majority of the Cenozoic (Galloway et al., 2000). This lack of fluvial input, and thus sediment loading, has been attributed to the area being an immature primary basin. Although the study area is mainly a sediment-starved basin, peak deposition occurred during the Miocene (Galloway et al., 2000). The Miocene depositional episode, largely attributed to the Tennessee River (Combellas-Bigott et al., 2006), initiated movement of the Louann Salt in the study area, creating multifaceted salt structures. The resulting sea-floor topography influenced both the location and configuration of sediment transport systems and depocenters throughout the Cenozoic (Rowan et al., 1998). The present-day bathymetry of the study area shows high topographic relief where prominent topographic features relevant to this study, including three salt domes, can be observed.

The structural evolution of the Northern GOM basin throughout the Cenozoic was largely controlled by sediment progradation over allochthonous salt structures (Diegel et al., 1995; Ge et al., 1997). Overall, the depositional patterns of the GOM are determined by a combination of regional and local tectonics, sea level fluctuations, subsidence, and varying sediment supply (Posamentier et al., 2003). Subsidence is an important contributing factor in creating accommodation in the GOM, which allowed massive accumulation of sediments during its geologically short history and thus massive amounts of salt diapirism.

Methodology

The 3D seismic data consist of Random Noise Attenuation (RNA) pre-stack time-migrated data. The 64 fold seismic data have a bandwidth of 10 – 60 Hz and a dominant frequency of 20 Hz in the area of interest. The migration velocity (2158 m/s [7080 ft/s]) and instantaneous frequency (20 Hz) were used to calculate vertical resolution as 27 m (90 ft) and detection limit as 7 m (22 ft). Seven wells, along with their associated bypasses and sidetracks, were correlated. Biostratigraphic data as well as gammay ray, deep resistivity, density, conductivity and neutron porosity wireling logs were collected and analyzed for all wells. Well and wirleline log data aided in correlating coeval surfaces from both sides of the channel complex (Fig.3). Major erosional surfaces, constituting channel-complex bases, along with their coeval depositional surfaces were mapped as horizons 1 – 6, 1 being the oldest and 6 being the youngest horizons (Figs. 4 and 5).

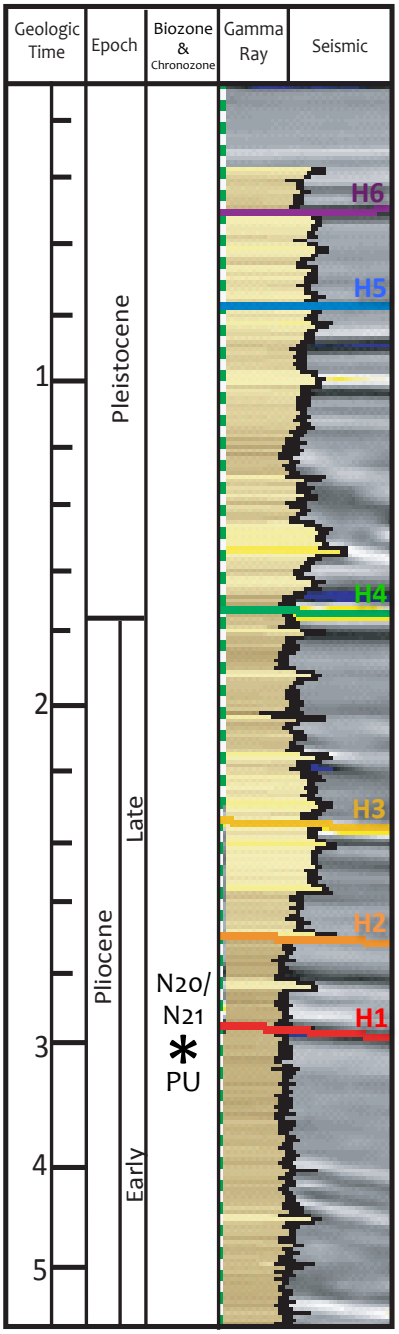

Figure 3. Gamma ray and seismic data for the interval of interest in study area. The lithologic column, based on gamma ray evaluations, depicts sand as yellow and shale as brown. Horizons utilized in the study are labeled here as H1 – H6. Collected paleomarker information locations are shown by star with the BOEMRE chronozone labeled below and the Standard Foraminifera Zone (Bolli et al., 1969, 1979) labeled above. Only one biozone marker fell within the area of interest, Sphaeroidinellopsis seminulina, a planktonic foraminifera from chronozone PU and biozone N20/N21, with a last occurrence of 3.16 my marking the beginning of the Late Pliocene. Paleontological well information according to BSEE website (https://www.data.bsee.gov/homepg/data_center/paleo/paleo.asp last access: 8/24/2015). Chronozone information according to BOEM website (https://www.data.boem.gov/homepg/data_center/gandg/ biochart.pdf last access: 10/2/2015)

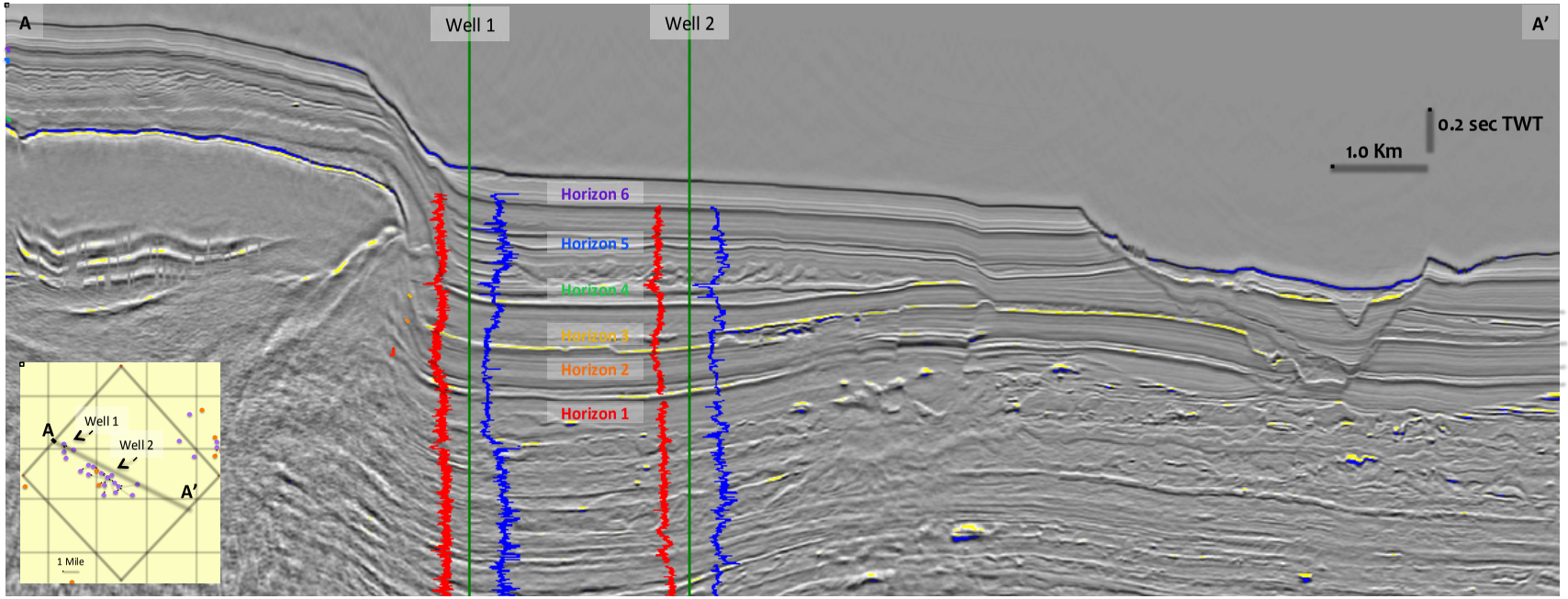

Figure 4. A representative seismic line with two wells and interpreted Horizons 1-6. Wells are shown with gamma ray logs to the left in red and resistivity logs to the right in blue. Extent of seismic data with relative location of seismic line outlined in red on base map, data extent is located within circle on figure 1.

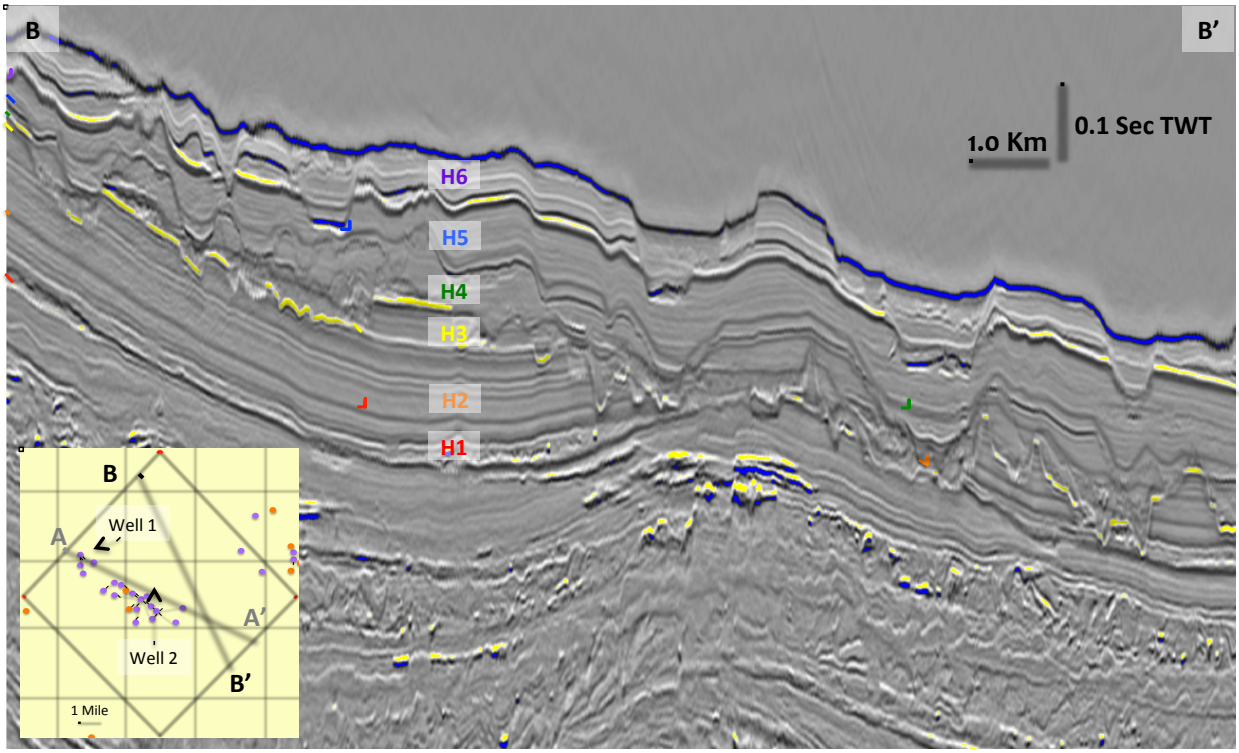

Figure 5. Dip Oriented Seismic Line. Seismic line B-B' shows the current slope of the sea floor and the six interpreted horizons of interest used in this study, labeled here as H1 –H6. Base map shows location of this seismic cross section in black, and the location of the seismic cross section A-A' (Fig. 4) in grey.

Isochron maps were created between each horizon and its adjacent horizon. Horizons were individually flattened, and seismic slices were created parallel to the flattened horizons, referred to here as horizon slices, along which seismic attributes were extracted. Attributes utilized include two-way travel time reflectivity and amplitudes, spectral decompositions, the instantaneous attributes: acceleration of phase, dominant frequency, instantaneous frequency, instantaneous phase, and trace envelope, as well as the geometric attributes: curvature azimuth, dip azimuth, instantaneous lateral continuity, and a shale indicator (Table 1).

Table 1. Summary of seismic attributes uses. Attributes have been divided into two categories with instantaneous attributes in green and geometric attributes in red.

	Attribute	Local - Both* - Regional	Depositional Environment	Bedding Indicators	Unconformities	Continuity/ Discontinuity	Lithology	Fault Detection	Fractures
Instantaneous	Acceleration of Phase	Loc					X		
	Dominant Frequency	Loc	X	X			X		X
	Instantaneous Frequency	Loc	X	X			X		X
	Instantaneous Phase	Loc	X			X			
	Trace Envelope (Reflection Strength)	Loc	X		X		X	X	
Geometric	Curvature Azimuth	Both*	X		X			X	X
	Dip Azimuth	Both*	X						
	Instantaneous Lateral Continuity	Both*	X	X		X		X	X
	Shale Indicator	Both*	X				X		

Spectral decomposition is the transformation of seismic data into discrete frequencies/ wavenumbers, and is used to identify stratigraphic variations, layer thickness and to determine lithologies. Acceleration of phase is locally used for lithology & absorption. Both the dominant frequency and instantaneous frequency are used as local indicators of depositional environment, bedding indicators, lithology and fractures. Instantaneous phase aids in detailed visualization of bedding configurations, and represents all events since it does not take amplitude into account. It is a local indicator for depositional environment, lateral continuity, sequence boundaries and as a discriminator for geometrical shape classifications. The trace envelope, or reflection strength, represents the total instantaneous energy of the complex trace independent of the phase, it is a local indicator for depositional environment, unconformities, faults and the spatial correlation to porosity and other lithologic variations. Curvature azimuth is used mainly to detect edges, which are associated with asymmetric (faults) and symmetric (ridges/valleys) surface features. Dip azimuth is a local and regional indicator for depositional environment. Instantaneous lateral continuity reflects the instantaneous curvature of seismic reflections and is used to detect the depositional environment, bedding indicators, continuity/discontinuity, fault detection and fractures on both the local and regional scale. Shale indicator is a local and regional indicator for depositional environment and lithology, designed to detect possible shale zones in a clastic environment.

Channels from each horizon slice were examined and parameters of meander morphology were measured (Fig. 6). These parameters were used to evaluate plan-form morphology of the channel at various geologic times. Salt movement was measured for the three salt domes within the confines of the dataset utilizing the Principle of Original Horizontality and the basis of back-striping. The uppermost horizon was flattened; subsequent horizons, which appeared flattened as

A.

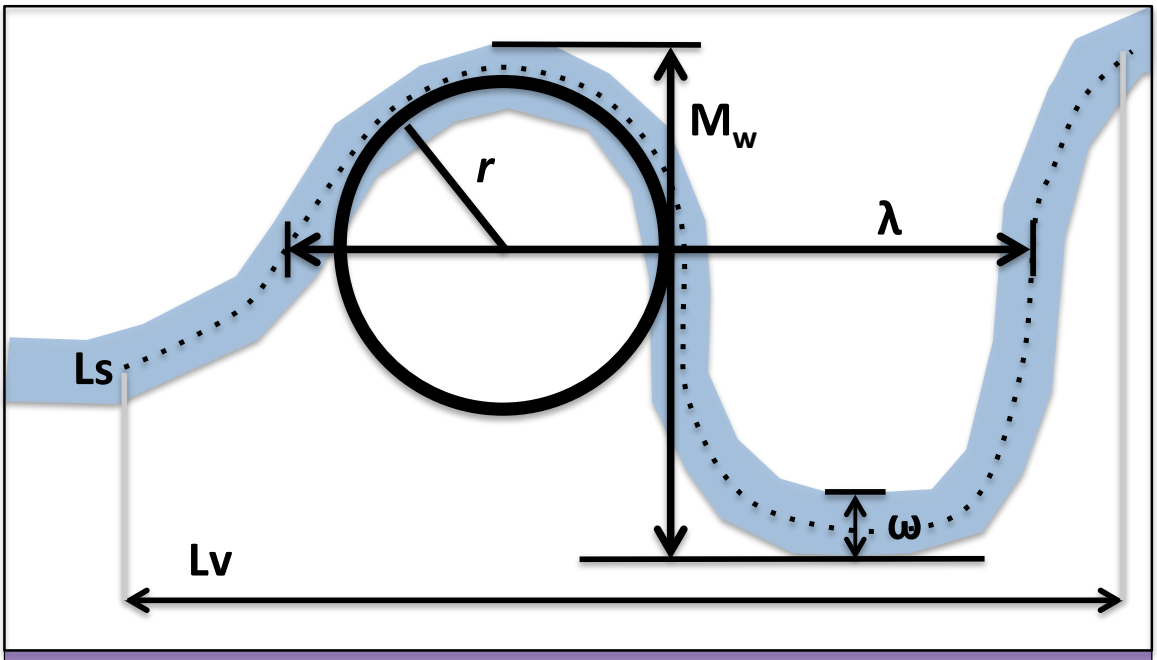

B.

Measured Properties	
Stream length (Ls)	Meander wavelength (λ)
Valley length (Lv)	Channel width (ω)
Meander bend radius (r)	Meander width (Mw)

C.

Calculated Properties		Reference:
Sinuosity (K)	K = (Ls) / (Lv)	Mueller 1968
Curvature ratio (C)	C = (r) / (ω)	Fagherazzi et al.,2004
Length-width ratio (L)	L = (λ) / (Mw)	Gornitz 1973

Figure 6. A. The geometric relationship of the morphology of a typical meandering channel (modified from Wood 2007). **B.** List of abbreviations for the measured meander properties (Wood 2007). **C.** Calculated variables of meander properties. The associated reference is given to the right of each equation.

well, indicated no salt movement during the time that those horizons were deposited. The youngest horizon that did not appear flat was then flattened, areas where this horizon was not parallel to its location in the previous flattened section was considered as areas affected by salt movement (Fig. 7). This process was repeated for every subsequent horizon down to Pliocene/Miocene boundary.

There are two approaches to study patterns in meandering bodies (Williams, 1986). The first approach focuses on the predictability of the geometric patterns displayed by meanders (Leopold et al., 1960), and the second approach focuses on attempting to explain the variability and oddities observed in the geometry of the meanders (Williams, 1986, after Ferguson, 1976). The relationships between measured variables were analyzed here using both methods.

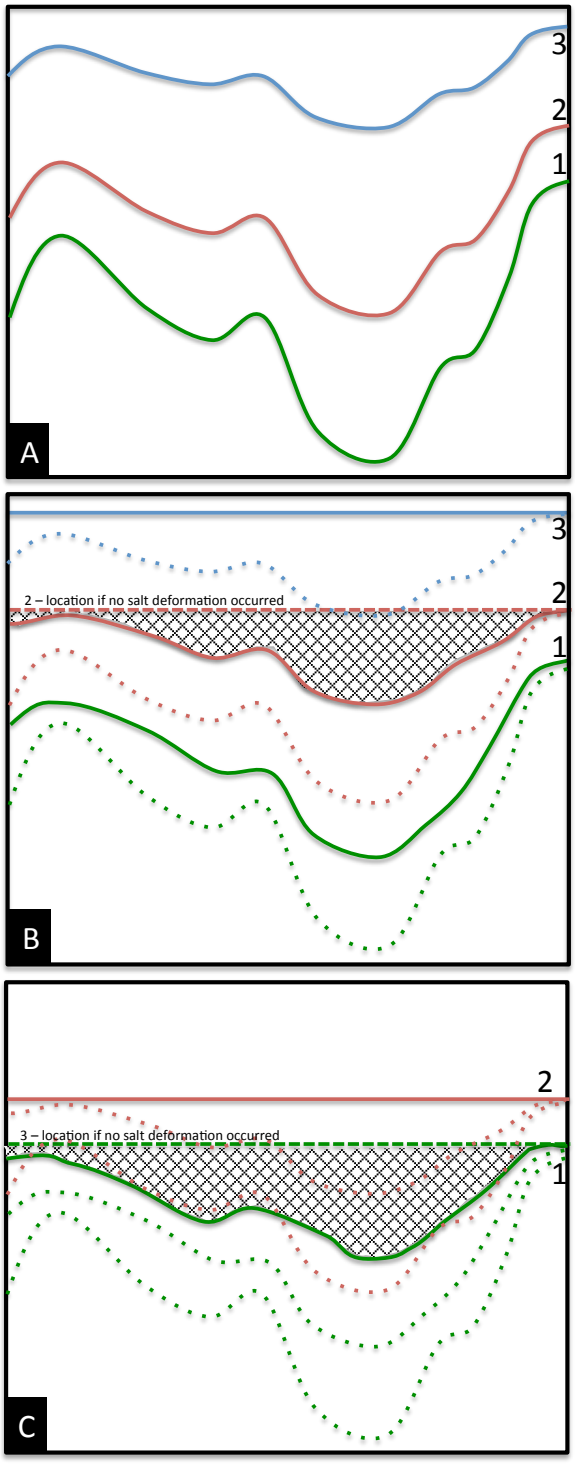

Figure 7. Definition diagram of method used to determine relative halokenetic movement between each interpreted horizon. Image A depicts the original position of various seismic horizons. Image B shows that if the uppermost horizon is flattened, horizons directly below also become parallel, labeled as unit 3. Horizons further below the uppermost horizon should also be parallel, as depicted by dotted line. The area below the parallel dotted line and the top of the next horizon is taken as the effect of salt movement. Image C depicts the effect of salt movement between unit 1 and 2 observed when unit 2 is flattened.

Results

The rate of halokinesis movement (Fig. 8) shows that during late Pliocene, all three salt domes were rising at faster rates compared to depositional rates in the surrounding areas. Salt movement started to slow down significantly at the beginning of Pleistocene. Salt domes 1, 2 and 3 show similar patterns of movement, most likely related to similar evacuation rates occurring during times of larger depositional episodes. Larger deposodes, despite their differential loading, created enough pressure to cause evacuation of the underlying salt into the 3 salt diapirs, thus creating more accommodation space and new topographic lows.

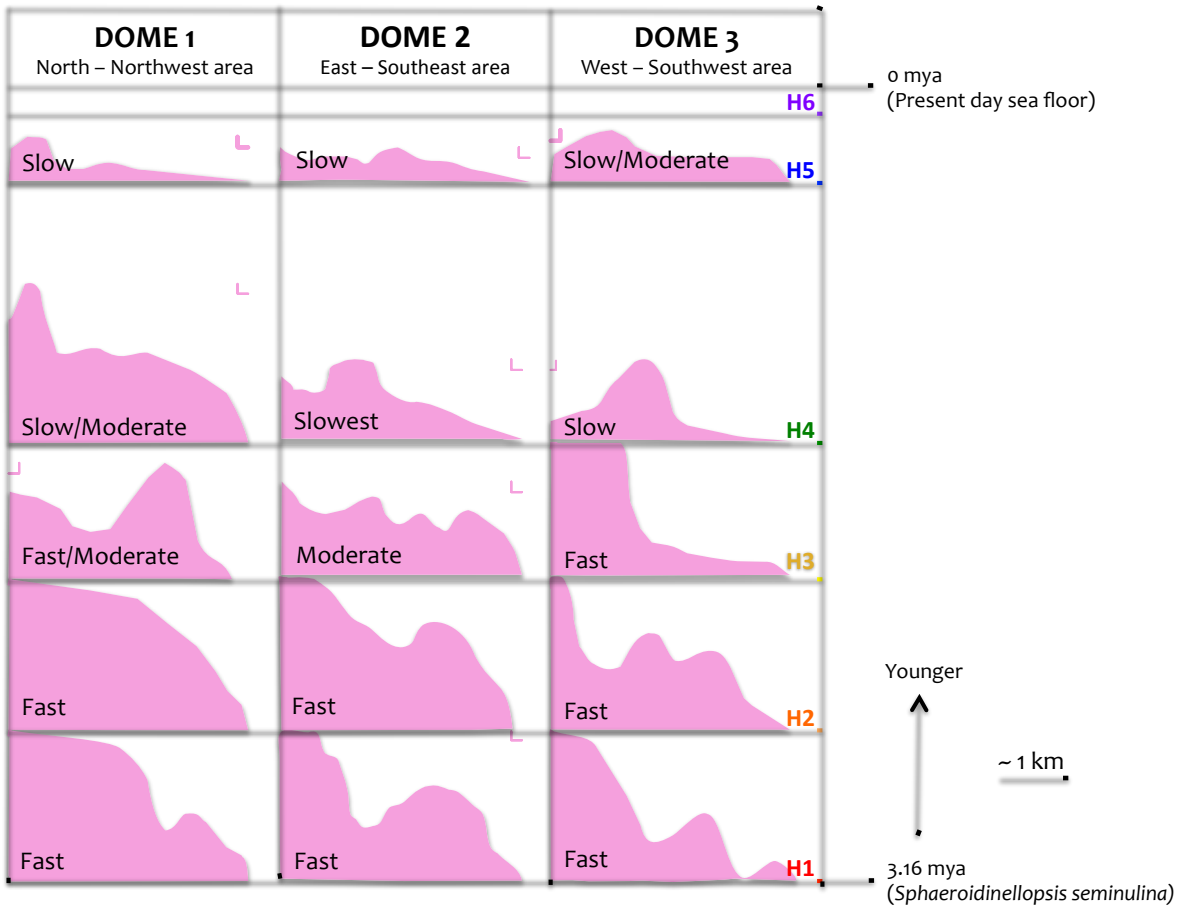

Figure 8. Relative salt migration vs. deposition. Horizons utilized in this study are labeled here as H1-H6. White area between Horizons represents relative amount of deposition. Pink areas represent relative amount of salt movement.

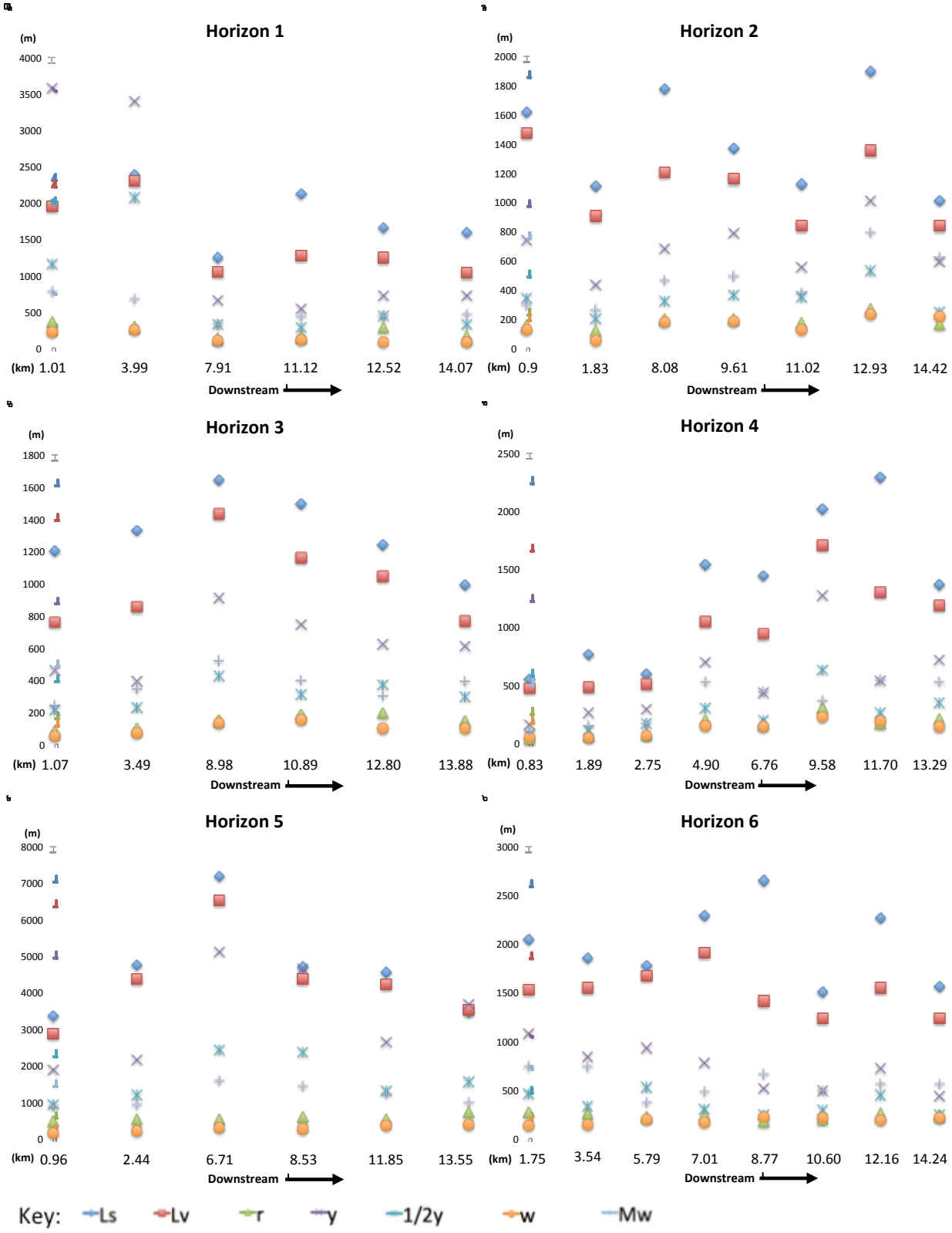

Figure 9. Downstream changes in all measured variables across all interpreted Horizons.

Downstream changes of all measured variables for channels identified in various horizon slices are shown in Figure 9. Submarine channels rarely display a braided morphology (Peakall 2015; Foreman et al., 2015), but in some studies conducted in the Labrador Sea, Santa Monica Basin (Hesse et al., 2001), and in De Soto Canyon, GOM (Posamintier 2003), braided and anastomosing patterns have been interpreted to occur in a deep water setting. Here, we have also considered the possibility of braiding when discussing the sinuosity of submarine channels.

Horizon 1: Fast, steep movement of Salt Dome 1 in the northern portion of the study area, created a valley that captured channels in a predominately straight morphology. Movement of Salt Dome 2 affected its surrounding topography as well, producing an inflection point in the mid-channel area where the slope levels out. Channels depict a more sinuous morphology in this area. As channels are diverted around Salt Dome 2, the slope decreases and conditions allow for a meandering morphology (Fig. 10A).

Between Horizon 1 – Horizon 2: Massive amounts of erosion in the downstream channel reaches are observed (Fig. 11A). Salt Dome 1 shows greater movement causing more sediment deposition in the adjacent area where accommodation was created.

Horizon 2: Channels evolved towards a state of more equilibrium, showing a sinuous morphology for its entirety. The sinuosity of the channel is relatively low (1.1 – 1.45), verging on the boundary of possible braiding. As Salt Dome 2 rises, it causes the topography on the east bank of the channels to have more relief. Cut banks on the east side depict higher erosions.

Evacuation of salt from areas surrounding Salt Dome 1 has caused the northern channel reaches to split into two distinct tributaries feeding the main channel (Fig. 10B).

Between Horizon 2 – Horizon 3: The majority of the downstream portions of the channels show erosion. Salt Dome 1 has significant salt evacuation and diapirism, which resulted in the northern area having more salt withdrawal and adding accommodation space, showing massive amounts of deposition. Salt Domes 2 and 3 show less movement than Salt Dome 1, causing the southern portion of the study area to accrue only minor amounts of sediment deposition (Fig. 11B).

Horizon 3: Channels in north meanders due to a decrease in slope caused by preceding depositional phase in the surrounding area. The remainder of the channels continues to show a lower sinuous morphology, with a possibility of braiding. This lower sinuosity in the south is due to the slowing movement of Salt Dome 2, as seen by the offlap surfaces. Salt Dome 1 movement has slowed as well, but to a lesser extent (Fig. 10C).

Between Horizon 3 – Horizon 4: The entire channelized area shows large amounts of erosion. The eastern portion of the study area lacked significant deposition in this interval, whereas the southwestern part became the focus of deposition. This shift in basin depocenter was due to the slowed rates of diapirism in Salt Dome 2, the relatively faster movement of Salt Dome 1 and the continued fast movement of Salt Dome 3 (Fig. 11C). This prompted deposition between these two domes.

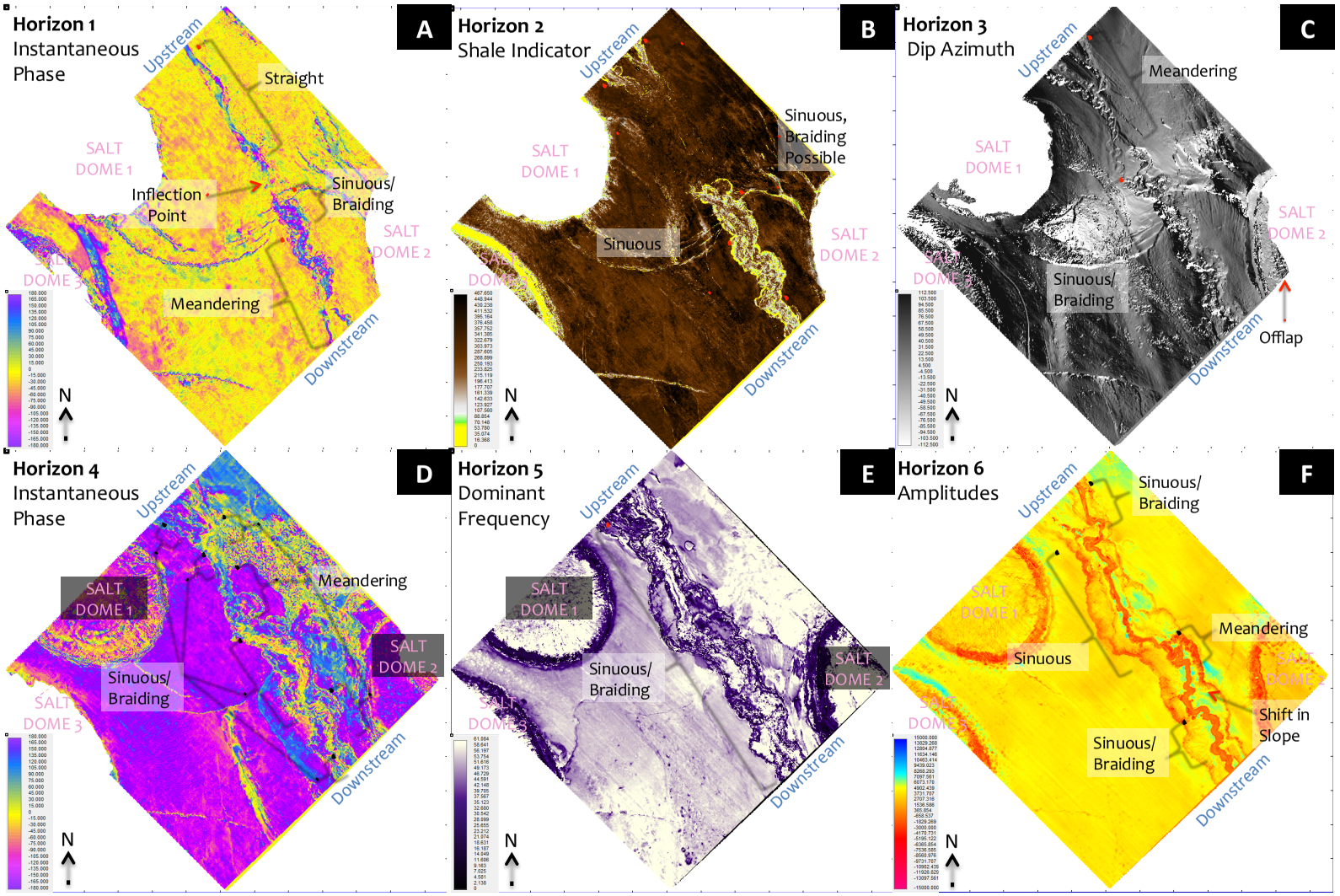

Figure 10. Horizon slices for all interpreted horizons with each displaying a different seismic attribute. Each horizon slice reveals submarine channels with varying morphology.

Horizon 4: Channels continue to move towards equilibrium. Channel morphology alternates between meandering and sinuous. All the measured variables (Fig. 9) show a general increasing trend towards downstream until channels are at the foot of Salt Dome 2, where they began to spread (Fig. 10D). Movement of Salt Dome 1 and 2 have slowed, as seen by the deposition on top of these domes.

Between Horizon 4 – Horizon 5: Channels begin to show preserved levees, which cease with the beginning of Horizon 5 deposition. The depocenter shifts from the southwestern to the northwest part of the study area due to non-uniform diapirism rates in Salt Dome 1 (Fig. 11D). Both Salt Dome 2 and 3 slowed their movements.

Horizon 5: Channels reached an equilibrium state, most likely from the sufficient time to adjust as the salt movement slowed significantly. The slope of the area adjusted as well, becoming less steep and shallower. It is for this reason that the sinuosity of the channel as a whole decreased. While the sinuosity is low enough that braiding could occur throughout, braiding is unlikely to have occurred due to the lower slope during this time (Fig. 10E). With these changes, both the meander radius and channel width became highest, with both variables slightly increasing downstream.

Between Horizon 5 – Horizon 6: Channel erosion occurs mainly on the cut bank side of the channels. The infilling of the channels is due to abandonment, which occurs immediately following Horizon 5 (Fig. 11E). The abandonment surface can be linked to ceased salt movement in Salt Dome 2. The following reactivation surface occurs immediately before Horizon 6. This

reactivation surface is generated as the rate of salt movement in Salt Dome 2 and Salt Dome 3 increases. The deposition in the study area changed from basin fill to wedge fill and followed the current shelf-edge break.

Horizon 6: The entire channel is again out of equilibrium, without multiple tributary channels. Near Salt Dome 1, where salt movement was still decreasing, the slope became gentler. This decrease in slope corresponds to a downstream increase in sinuosity for the northern part of the channels (Fig. 10F). Due to the reactivation of salt movement in Salt Dome 2, there is a local 90° shift in slope direction, as well as a local increase in slope. These led to a decrease in channel sinuosity.

Horizon 6 – Seafloor: The study area shows basin has consistent deposition throughout, creating a moderate slope. The channel underwent more erosion on the southern cutbanks, whereas the northern cutbanks shows erosion only on the cutbank edges of the overbank area (Fig. 11F). Depositional packages on the edges of the salt domes are thinned, indicating coherent salt movement. Channels begin to move back towards an equilibrium state.

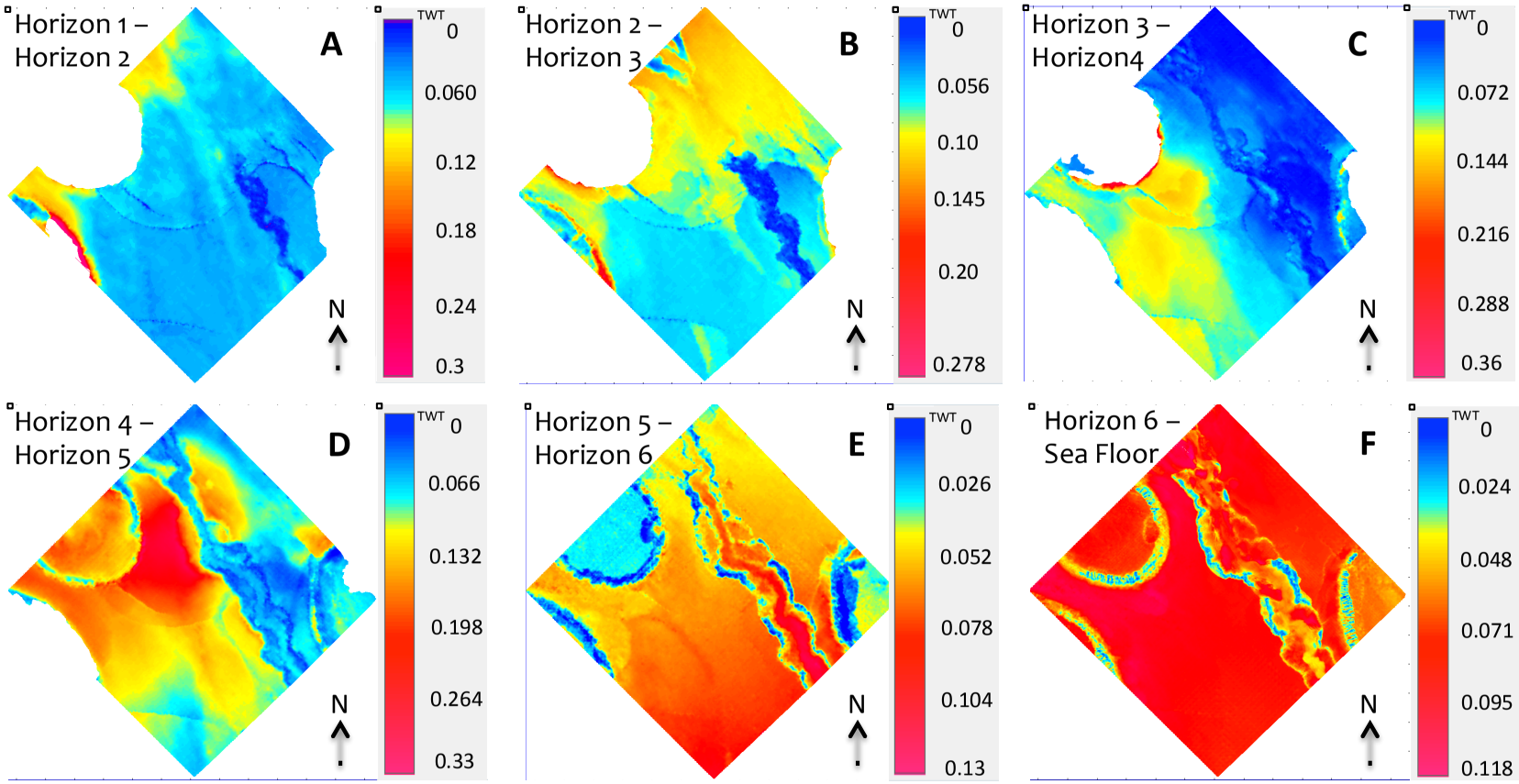

Figure 11. Isochrons depicting the difference in two way travel times between two successive horizons. Blue areas indicate thinner and red areas indicate thicker deposits.

Discussion

Overall, the morphology of our submarine channels is consistent with previous studies on sinuous submarine channels in areas not affected by halokinetics. The sinuosity of the channels thalweg ranges from straight to meandering (Fig. 13A), however when looking at the overbank area, there is a distinct lack of sweep (Fig. 12). This sweep/swing geometric pattern partially disagrees with findings proposed by Posamentier et al. (2003), who indicate significant downstream meander loop migrations for both the channel and overbank area of submarine

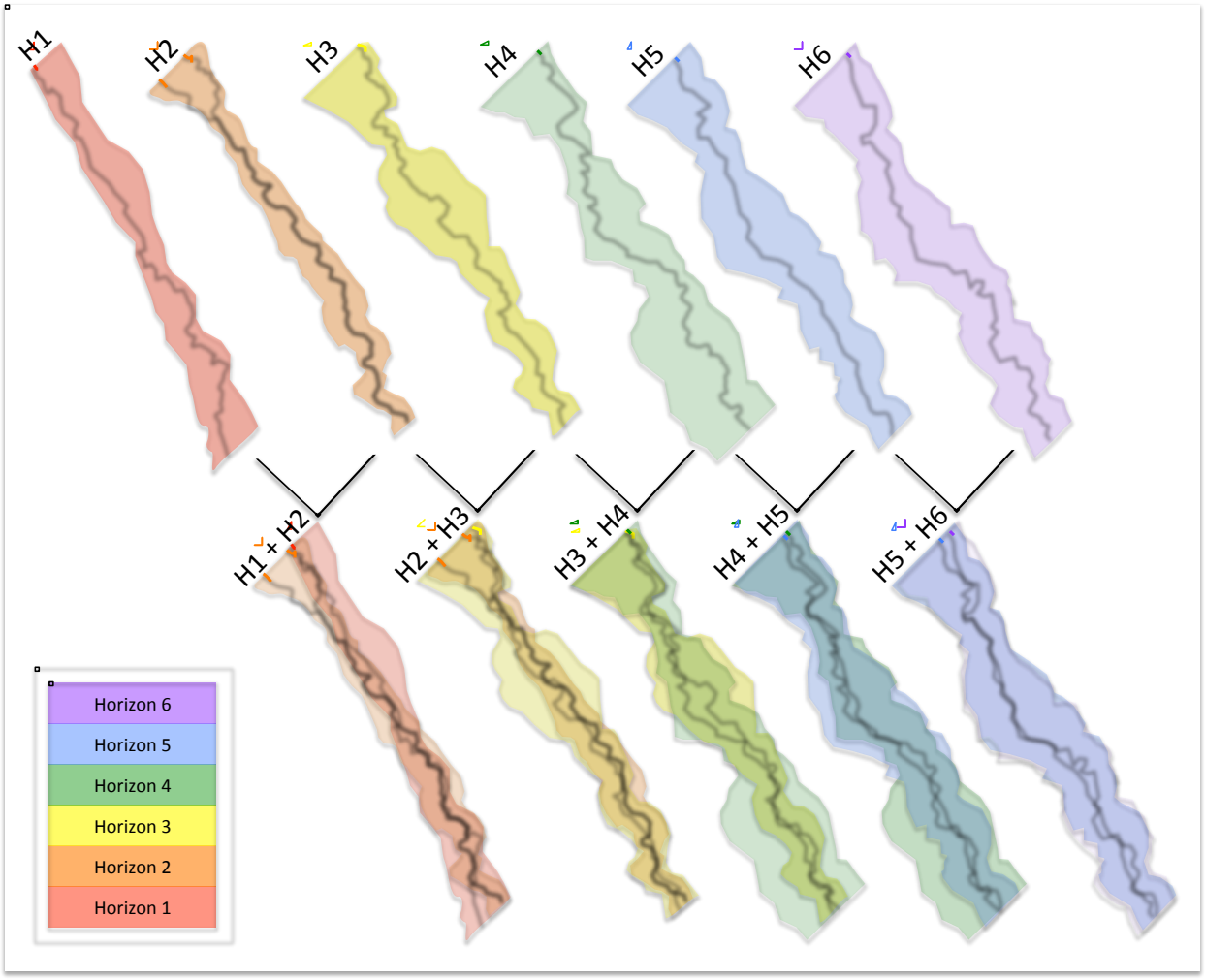

Figure 12. Planform channel morphology for various horizons. Channels for each horizon are depicted by thick solid line, the areal limit of overbank area associated with each horizon is outlined and filled transparently with the same color. Horizons are stacked below, showing changes between all horizons concurrently. Note distinct changes in channel morphology while general pattern of overbank area remains consistent.

channels in the GOM, however this disagreement may be due to either the smaller size of the channels used in this study or to the topographic influence of salt domes. The findings of this study adhere more closely to conclusions drawn by Peakall et al. (2000), who argued that meanders in deep-water settings show a lack of sweep and that sinuosity can develop through limited lateral migration, however this pattern is not seen in the actual channels of this study, but instead is only applicable to the observed overbank areas.

The sinuosity vs. the length/width ratio (Fig. 13A) indicates an overall negative exponential trend for each coeval channel, suggesting that channels are experiencing a significant decrease in slope within a very short distance. However, as channels evolve through time, the slope levels out, displaying unique morphologies as the study area gets rapidly filled. Horizon 3 depicts this by showing a meandering morphology further upstream than a sinuous morphology, which coincides with faster migration of salt domes before they begin to slow. Typical channels become more sinuous through time. Channels studied here are not simply becoming more sinuous as they evolve, most likely because lateral migration can be responsible for meander growth (Babonneau et al., 2010). While there is an inverse correlation between sinuosity and valley slope (Schumm, 1972; Schumm et al., 2000), stream power and sediment load can also affect sinuosity. Using channel wavelength plotted against meander width as a proxy for flow (Fig. 14; Nayak et al., 2010), all Horizons except Horizon 5 (and partly horizon 1) fall into the category of having a low meander width and low wavelength, suggesting a lower flow or "crenulous" system. Thus changes in sinuosity for Horizons 1 – 4 and Horizon 6 are likely due to the observed changes in slope. Horizon 5 has a low width and high wavelength, which is indicative of a straighter channel.

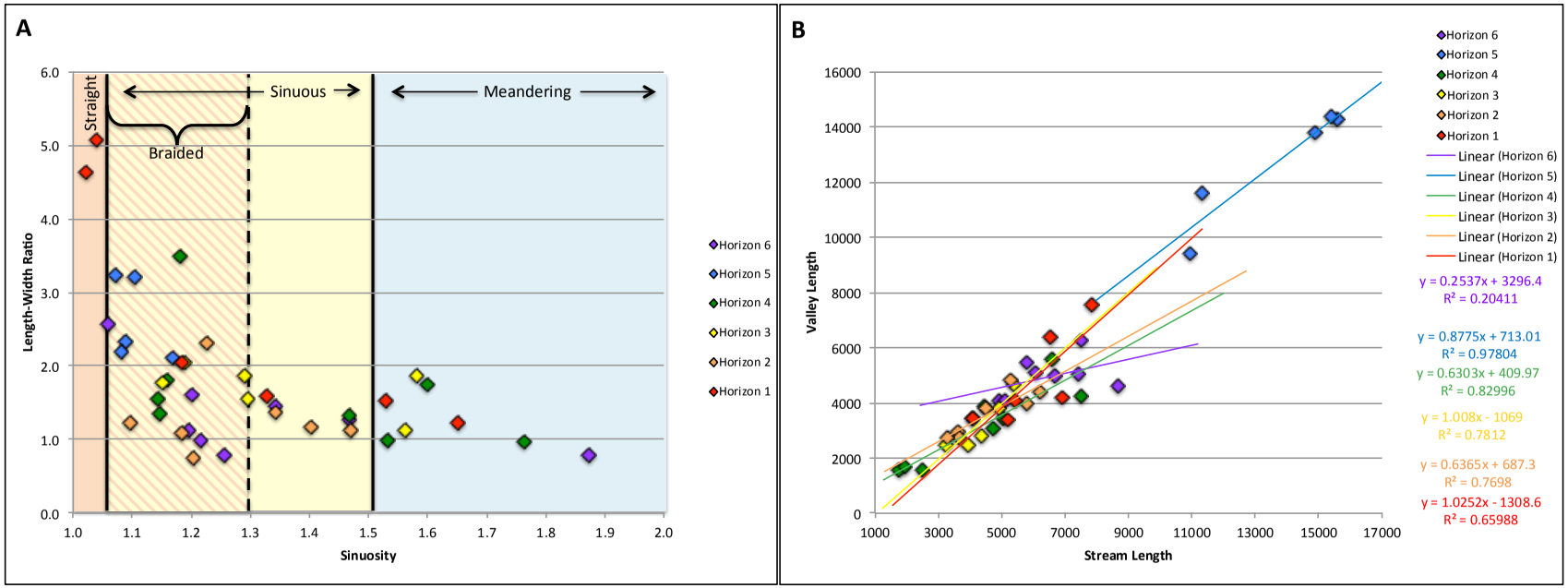

Figure 13. . A) Sinuosity plotted against length-width ratio for various measurement locations across all Horizons. The background has been colored to show Mueller's sinuosity index, where straight channels have a sinuosity of <1.05, sinuous channels have sinuosity 1.05-1.5, and meandering channels have sinuosity of >1.5. Channel braiding can occur at a sinuosity index of <1.3 (Ghosh et al. 2012). **B)** Stream length plotted against valley length for various measurement locations across all Horizons. The more linear trend lines indicate that the system is in equilibrium (Hackbarth and Shew 1994; Peakall et al., 2000). The graph illustrates that from Horizons 1 to 5, the channel system moves towards an equilibrium state with time. Horizon 6 shows a system in disequilibrium.

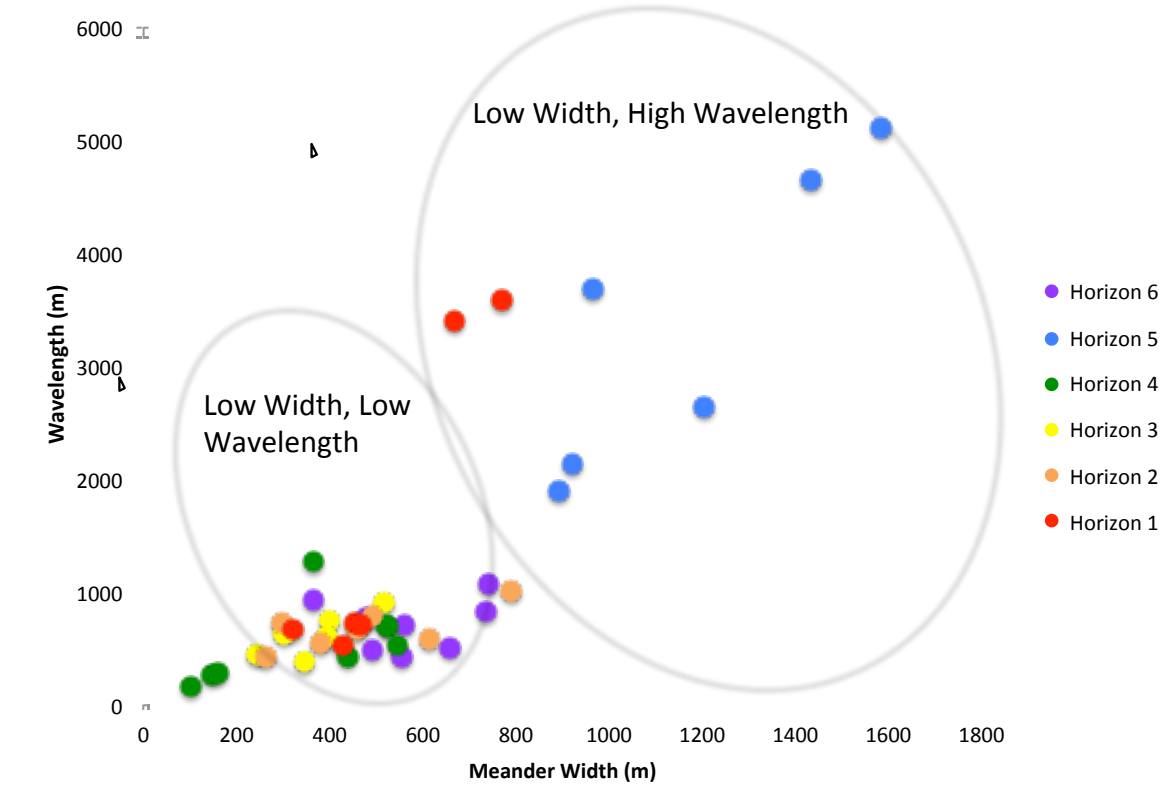

Figure 14. Meander width plotted against wavelength. Areas with low meander width and low wavelength represents a slow flow or crenulous system. Areas with low width and a high wavelength represent a straighter system. High/low cutoffs modeled after Nayak et al., 2010. The high width, high wavelength areas occur beyond the confines of this graph.

As halokinetic rates slow, channels move towards a state of stability due to decreasing slope. According to previous studies (Hackbarth and Shew 1994; Peakall et al., 2000) when stream length is plotted against valley length for a channel, a more linear trend line indicates a system with more stability, or a system in equilibrium. After the development of initial sinuosity there is a trend of increasing channel stability towards plan-form equilibrium (Hackbarth and Shew 1994; Peakall et al., 2000). Measurements of stream length plotted against valley length (Fig. 13B) indicate that the channel moves towards an equilibrium state until reinitiation of halokinesis occurs following deposition of Horizon 5. Contemporaneous slowing, and

subsequent halting, of salt diapirism and channel advancement towards an equilibrium state are evident from the consistent sinuosity observed in Horizon 5, which occurs immediately before channel abandonment. Reactivation of salt diapirism prompts channel reactivation. As a result, channel morphology quickly adapts due to slope change, and channels are thrown into a state of disequilibrium, as seen by the morphology of Horizon 6 (Fig. 10F). Stream length and valley length are affected during this change in morphology, leading to a fluctuating state of stability that is dependent upon the salt movement.

When comparing meander radius to wavelength (Fig. 15), there is little correlation of organized movement with time. However, there is a distinct linear trend. When compared to previous studies (Clark et al., 1992 after Leopold and Wolman, 1960), our data fall below the regression line for submarine channels but along the regression line for fluvial channels. This implies that the meanders of our submarine channels have a tighter curvature than average submarine channels with lower wavelengths and smaller radii. Previous studies have shown that for submarine channels with wavelengths of < 5000 m (Nayak et al., 2010), it is possible to get a meander geometry which is more fluvial-like. That is, smaller submarine channels can display more curvature in meander bends than what is expected in larger submarine channels.

Strong entrenchment during channel incision can suppress overflow (Babonneau et al., 2010). Entrenchment in the study area increases from Horizon 1 to Horizon 5, with less possibility of overflow as the channel evolves through time. Channels most likely developed a confined flow during deposition of Horizons 3 and 4. Confined portions of flow are known to behave more sinuously (Dykstra et al., 2009) that can help explain the increased values of

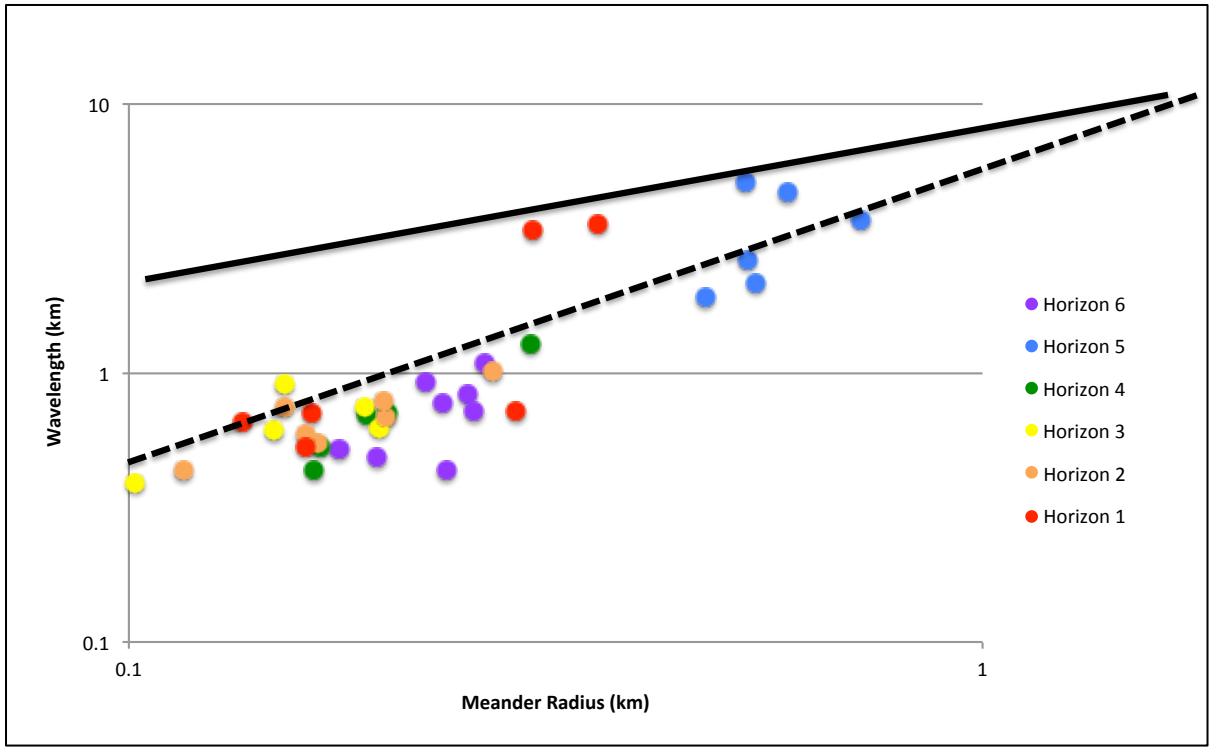

Figure 15. Meander radius vs. wavelength on a log-log scale, plotted on top of regression lines from Clark et al., 1992. Solid regression line represents submarine channel data from 16 fan complexes (Clark et al., 1992). Dashed regression line represents empirically derived fluvial channel data (Clark et al., 1992 after Leopold and Wolman, 1960).

sinuosity observed in Horizons 3 and 4. However, larger entrenchment can also lead to a decrease in sinuosity (Babonneau et al., 2010). The level of entrenchment was the highest immediately before the deposition of Horizon 5 and coincides with the highest rates of salt diapirism and evacuation. This increase in entrenchment, along with a subsequent decrease in slope caused by the cessation of salt movement, most likely caused the height of the velocity maximum of flow to increase (Serchi et al., 2011), suggesting that when Horizon 5 was deposited the flow was no longer confined.

Conclusions

As meandering submarine channels become entrenched in their path, local changes in seascape have little impact on overall channel location. Channel overbank areas show a lack of sweep and low rates of swing as they evolve through time. Local changes in seabed topography have a small effect on channel location and morphology, such as position and intensity of individual meander loops, and sinuosity index. On the other hand, the rate of salt diapirism, as expressed in terms of seabed topography and slope, has a profound impact on sinuosity and morphology of submarine channels. As halokinetics decreases, channels are able to move towards an equilibrium state. Termination of halokinetic movement can lead to channel abandonment due to decrease in slope caused by basin infilling. Reactivation of halokinetics can lead to the reactivation of a partially filled abandoned channel. The reactivated channel shows varying states of disequilibrium. Sea level changes likely had little effect on the studied system.

The finding that submarine channel morphology can be solely controlled by halokinetics has implications for petroleum exploration targeting deepwater channelized systems. This study can help reduce risks in predicting lithology, thus porosity, seal, and connectivity of a targeted channel system because depositional styles and preserved facies are linked to channel geometry through spatial distribution of depositional landforms and environments. Aggradational patterns and channel preservation are both greatly impacted by morphology and sinuosity of a channel such that changes in morphology can result in modifications of depositional facies distribution in both lateral and vertical directions. Because submarine channel morphology/sinuosity can be solely affected by rates of salt diapirism, it is important to gain a better understanding of local halokinetics and its relation to these dynamic meandering channels.

References

Babonneau, N., B. Savoye, M. Cremer, and M. Bez, 2010, Sedimentary Architecture in Meanders of a Submarine Channel: Detailed Study of the Present Congo Turbidite Channel (Zaiango Project): Journal of Sedimentary Research, 80, 852–866.

Bolli, H., J. Saunders, and K. Perch-Nielsen, 1969, 1979, eds., Plankton Stratigraphy: Cambridge, Cambridge University Press, p. 17-86.

Clark, J.D., N.H. Kenyon, and K.T. Pickering, 1992, Quantitative analysis of the geometry of submarine channels: Implications for the classification of submarine fans: Geology, 20, 633-636.

Combellas-Bigott, R.I., and W.E. Galloway, 2006, Depositional and Structural evolution of the middle Miocene depositional episode east-central Gulf of Mexico: AAPG Bullet, 90, 335- 362.

Damuth, J.E., R.D. Flood, R.O. Kowsmann, R.H. Belderson, and M.A. Gorini, 1988, Anatomy and Growth Pattern of Amazon Deep-Sea Fan as Revealed by Long-Range Side-Scan Sonar (GLORIA) and High-Resolution Seismic Studies: American Association of Petroleum Geologists Bulletin, 72, 885-911.

Deb, M., D. Das, and M.Uddin, 2012, Evaluation of Meandering Characteristics Using RS & GIS of Manu River: Journal of Water Resource and Protection, 4, 163-171.

Diegel, F. A., J. F. Karlo, D. C. Schuster, R. C. Shoup, and P. R. Tauvers, 1995, Cenozoic structural evolution and tectono-stratigraphic framework of the northern Gulf coast continental margin, in M. P. A. Jackson, D. G. Roberts, and S. Snelson, eds., Salt tectonics: a global perspective: AAPG Memoir 65, 109–151.

Dykstra, M., and B. Kneller, 2009, Lateral accretion in a deep-marine channel complex: implications for channellized flow processes in turbidity currents: Sedimentology, 56, 1411-432.

Fagherazzi, S., E. Gabet, and D. Furbish, 2004, The Effect of Bidirectional Flow on Tidal Channel Planforms: Earth Surf. Process. Landforms Earth Surface Processes and Landforms, 29.3, 295-309.

Ferguson, R.I., 1976, Disturbed periodic model for river meanders: Earth Surface Processes and Landforms, 1, 337-347.

Foreman, B. Z., S. Y. J. Lai, Y. Komatsu, and C. Paola, 2015, Braiding of Submarine Channels Controlled by Aspect Ratio Similar to Rivers: Nature Geoscience, 8.9, 700-703.

Galloway, W.E., P.E. Ganey-Curry, X. Li, and R. T. Buffler, 2000, Cenozoic depositional history of the Gulf of Mexico basin: AAPG Bulletin, 84, 1743–1774.

Galloway, W.E., 2008, Depositional evolution of the Gulf of Mexico sedimentary basin, in Hsü, K.J., ed., Sedimentary basins of the world, Volume 5, The sedimentary basins of the United States and Canada, Miall, A.D., ed.: The Netherlands, Elsevier, 505–549.

Gamboa, D., T.M. Alves, and J. Cartwrite, 2012, A submarine channel confluence classification for topographically confined slopes: Marine and Petroleum Geology, 35, 176-189.

Ge, H, M.P.A. Jackson, B.C. Vendeville, 1997, Kinematics and Dynamics of Salt Tectonics Driven by Progradation: AAPG Bulletin, 81, 398-423.

Gee, M.J.R., R.L. Gawthorpe, 2006, Submarine channels controlled by salt tectonics: Examples from 3D seismic data offshore Angola: Marine and Petroleum Geology, 23, 443–458.

Gee, M.J.R., R.L. Gawthorpe, K. Bakke, and S.J. Friedmann, 2007, Seismic Geomorphology and Evolution of Submarine Channels from the Angolan Continental Margin: Journal of Sedimentary Research, 77, 433–446.

Ghosh, S., and B. Mistri, 2012, Hydrogeomorphic Significance of Sinuosity Index in Relation to River Instability: A Case Study of Damodar River, West Bengal, India: International Journal of Advances in Earth Sciences, 1.2, 49-57.

Gornitz, V., 1973, The Origin of Sinuous Rilles: The Moon, 6, 337-56.

Hackbarth, C.J., and R.D. Shew, 1994, Morphology and stratigraphy of a mid-Pleistocene turbidite leveed channel from seismic, core and log data, northeastern Gulf of Mexico, in Weimer, P., Bouma, A.H., and Perkins, B.F., eds., Submarine Fans and Turbidite Systems: SEPM, Gulf Coast Section, 15th Annual Research Conference, 127–133.

Hesse, R., I. Klaucke, S. Khodabakhsh, D. Piper, W. Ryan, and NAMOC Study Group, 2001, Sandy Submarine Braid Plains: Potential Deep-water Reservoirs: AAPG Bulletin, 85, 1499-1521

Konyukhov, A.I., 2008, Geological Structure, Evolution Stages, and Petroliferous Complexes of the Gulf of Mexico Basin: Lithology and Mineral Resources, 43, 380–393.

Leopold, L.B., and M.G. Wolman, 1960, River Meanders: Geological Society of America Bulletin, 71, 769-794.

Loncke, L., V. Gaullier, J. Mascle B. Vendeville, and L. Camera, 2006, The Nile deep-sea fan: An example of interacting sedimentation, salt tectonics, and inherited subsalt paleotopographic features: Marine and Petroleum Geology, 23, 297–315.

Mancini, E.A., B.H. Tew, R.M. Mink, S.D. Mann, and B.L. Bearden, 1991, Geologic Framework of Norphlet and Pre-Norphlet Strata of the Onshore and Offshore Eastern Gulf of Mexico Area: Reprint from Gulf Coast Association of Geological Societies Transaction, 41, 590-600.

Milkov, A.V., E. Goebel, L. Dzou, D.A. Fisher, A. Kutch, N. McCaslin, and D. F. Bergman, 2007, Compartmentalization and time-lapse geochemical reservoir surveillance of the Horn Mountain oil field, deep-water Gulf of Mexico: AAPG Bulletin, 91, 847–876.

Mondelli, K., 2011, Salt Reconstruction and Study of Depositional History, Upper Jurassic, East Texas Basin: M.S. thesis, University of Houston.

Mueller, J., 1968, An Introduction to the Hydraulic and Topographic Sinuosity Indexes: Annals of the Association of American Geographers, 58, 371-385.

Nayak, S., R. Bastia, D. Guchhait, and D. Bhawal, 2010, Quantitative Seismic Geomorphology of Deepwater Slope Channels using Bathymetry Data: A Case Study from Offhsore Cauvery Basin, East Coast of India: 8th Biennial International Conference and Exposition on Petroleum Geophysics, SPG, Extended Abstracts, P-331.

Nelson, H., J. Damuth, H. Olson, and C. Escutia, 2010, Factors Controlling Modern Submarine Fan Architecture and Implications for Paleogene to Miocene Petroleum Plays in the Gulf of Mexico: Presented at the 2010 Annual Convention and Exhibition, AAPG.

Peakall, J., B. McCaffrey, and B. Kneller, 2000, A Process Model for the Evolution, Morphology, and Architecture of Sinuous Submarine Channels: The Journal of Sedimentary Research, 70, 434–448.

Peakall, J., 2015, Geomorphology: Undersea river patterns: Nature Geoscience, 8, 663–664.

Pilcher, R. S., B. Kilsdonk, and J. Trude, 2011, Primary basins and their boundaries in the deep-water northern Gulf of Mexico: Origin, trap types, and petroleum system implications: AAPG Bulletin, 95, 219–240.

Pindell, J., K. James, and M, Lorente, 2009, The Origin and Evolution of the Caribbean Plate: Geological Society, London, Special Publications, 328, 219 – 293.

Posamentier, H.W., and V. Kolla, 2003, Seismic Geomorphology and Stratigraphy of Depositional Elements in Deep-Water Settings: The Journal of Sedimentary Research, 73, 367–388.

Rowan, M.G., and P. Weimer, 1998, Salt-Sediment Interaction, Northern Green Canyon and Ewing Bank (Offshore Louisiana), Northern Gulf of Mexico: AAPG Bulletin, 82, 1055–1082.

Rowan, M. G., 2014, Passive-margin salt basins: hyperextension, evaporite deposition, and salt tectonics: Basin Research, 26, 154–182.

Schumm, S.A., and H.R. Khan, 1972, Experimental Study of Channel Patterns: Geological Society of America Bulletin, 83, 1755-1770.

Schumm, S. A., J. F. Dumont, and J. M. Holbrook, 2000, Active tectonics and alluvial rivers: New York, Cambridge University Press.

Serchi, F.G., J. Peakall, D. B. Ingham, and A. D. Burns, 2011, A unifying computational fluid dynamics investigation on the river-like to river-reversed secondary circulation in submarine channel bends: Journal of Geophysical Research, 116, 1-19.

Snedden, J.W., W. Galloway, T. Whiteaker, and P. Ganey-Curry, 2012, Eastward Shift of Deepwater Fan Axes During the Miocene in the Gulf of Mexico: Possible Causes and Models: GCAGS Journal, 1, 131–144.

Williams, G.P., 1986, River Meanders and Channel Size: Journal of Hydrology, 88, 147-164.

Wood, L.J., 2007, Quantitative Seismic Geomorphology of Pliocene and Miocene Fluvial Systems in the Northern Gulf of Mexico, U.S.A.: The Journal of Sedimentary Research, 77, 713–730.

Wu, S., P.R. Vail, and C. Carmez, 1990, Allochthonous salt, structure and stratigraphy of the north-eastern Gulf of Mexico. Part 1: Stratigraphy: Marine and Petroleum Geology, 7, 318-333.

Appendix A: Seismic Data Set

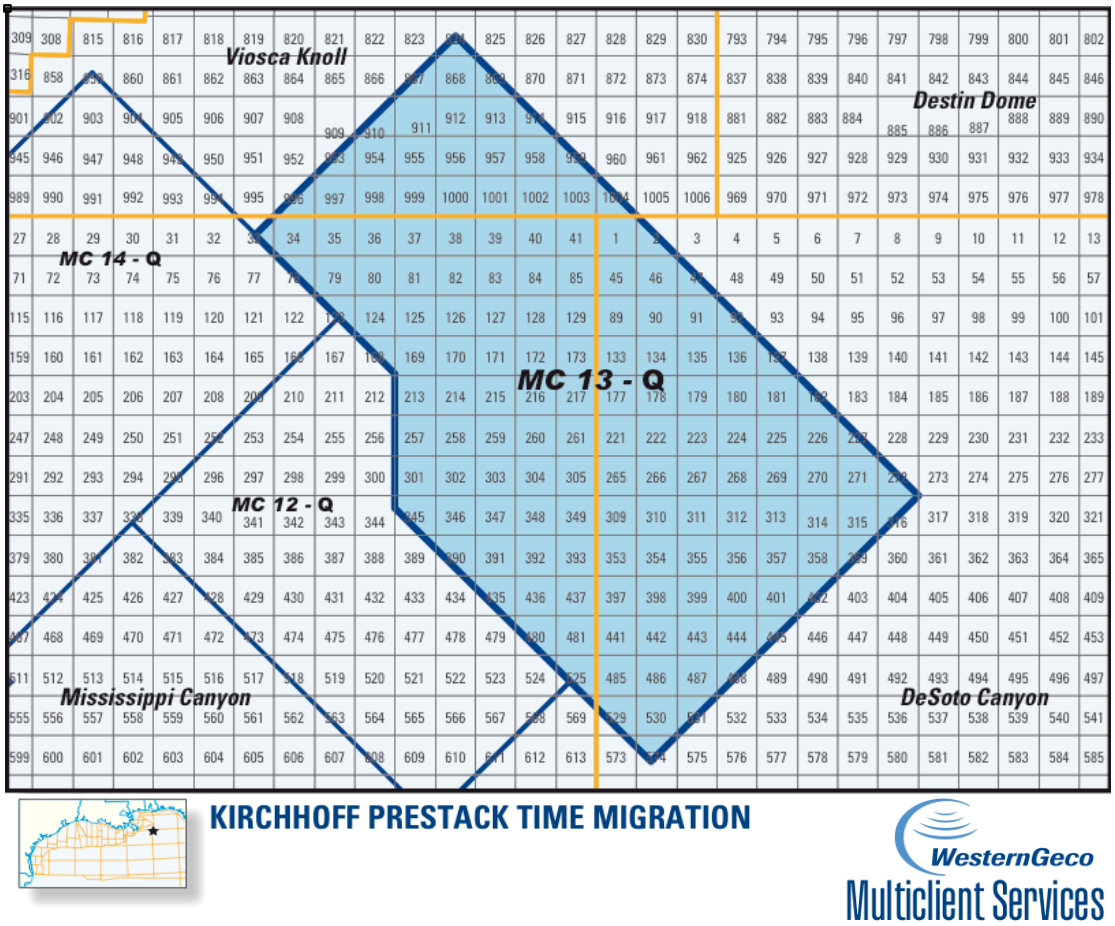

Figure A1. Data coverage of seismic survey Mississippi Canyon 13 – Q, Western Geco. Area of obtained data resides within this highlighted area.

Table A1. Acquisition Parameters of Seismic MC 13-Q , the 3-D seismic utilized in this study.

Recording System	Q-Marine* (Mark of Schlumberger)	Streamer Separation	100 m
Energy Source	Dual airgun arrays; 5085 $in.^3$	DGF Group Interval	12.5 m
Line Orientation	NW/SE	Sample Rate	2 ms
Source Separation	50 m	Record Length	12 s
Source Depth	5 m	Number of DGF Channels	640 per streamer
Shot Interval	31.25 m; 62.5 m per source; flip-flop	Nominal Fold	64
Streamer Depth	6 m	Final Bin Size	6.25 x 25 m
Streamer Length	8000 m	Survey Acquired	August, 2002

Table A2. Processing Flow of Seismic Survey utilized in this study.

Group forming
Navigation merge
CMS designature
Receiver motion correction
Noise attenuation
IMP/SRMA demultiple
Data reduction 6.25 m to 12.5 m
Radon demultiple
Water velocity correction
Q compensation (phase only)
Interpolation in crossline to 12.5 m spacing
Kirchhoff prestack time migration
CMS whitening
Stack
Poststack processing
Final cell size: 12.5 x 12.5 m
Final fold: 64
Final record length: 10 s
Final sample rate: 2 ms
Processing completed September, 2004

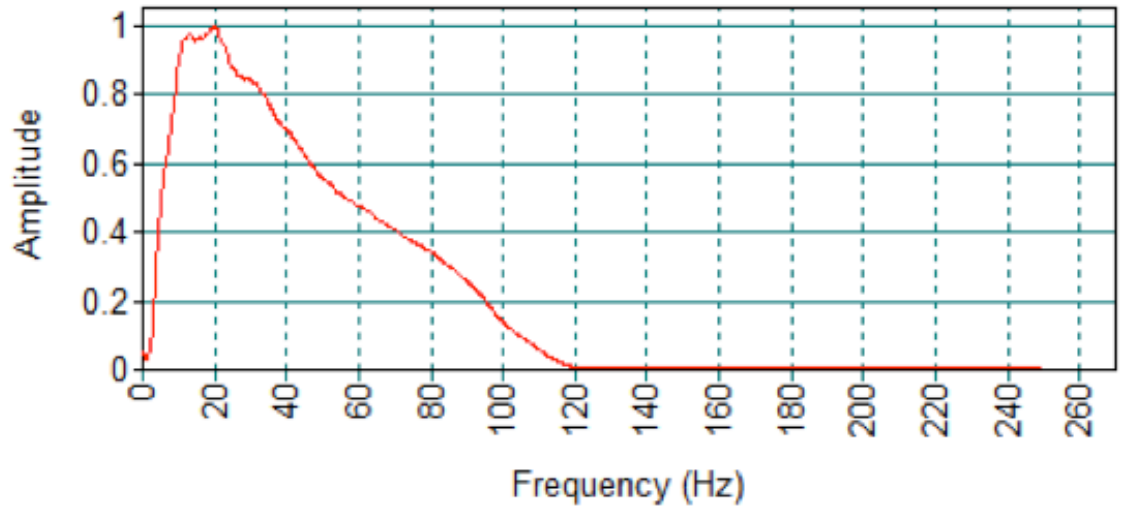

Figure A2. Frequency vs amplitude graph of the 3D seismic data showing a bandwidth of 10 – 60 Hz and a dominant frequency of 20 Hz.

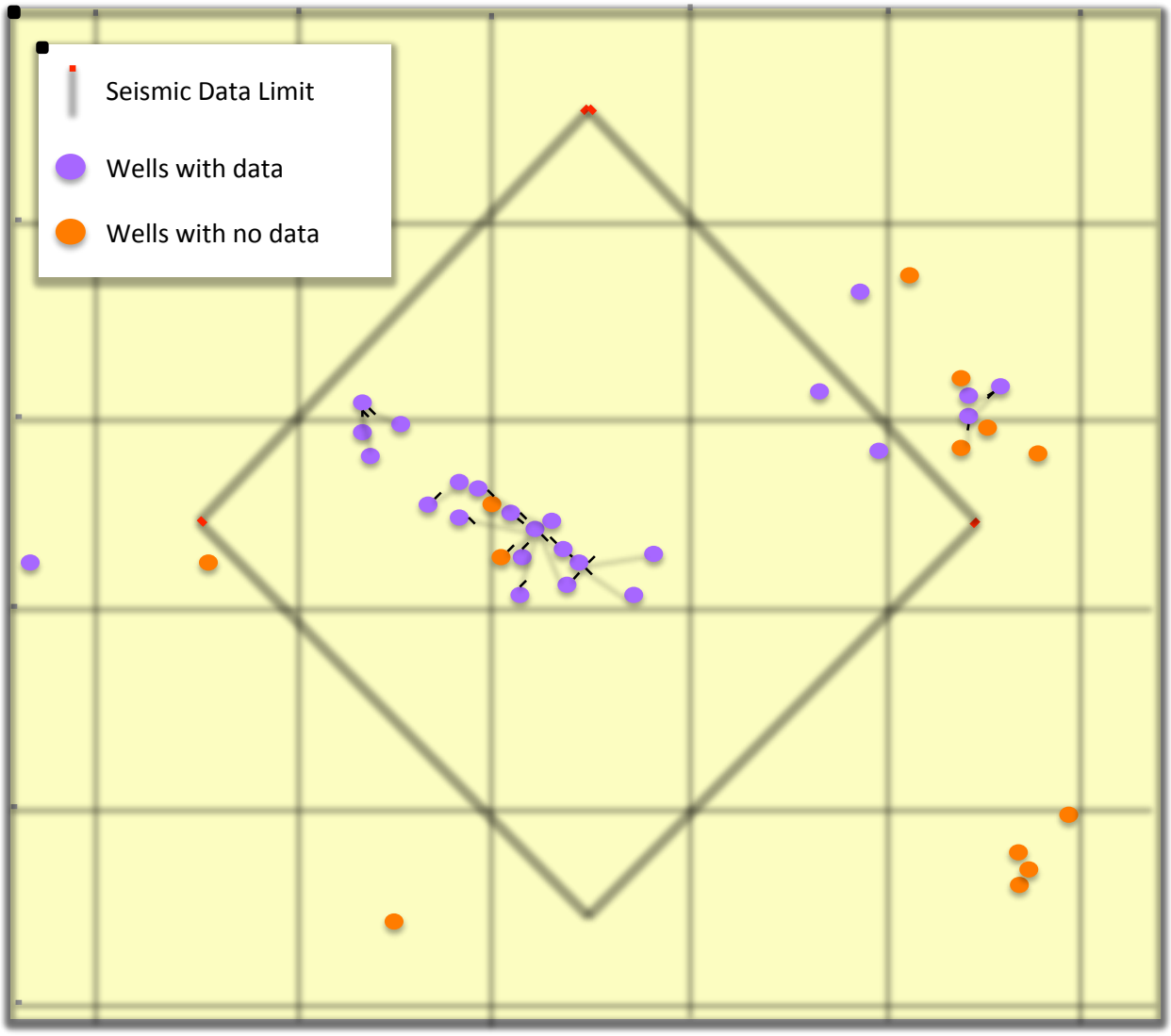

Figure A3. The extent of the acquired 3D seismic data is ~36 mi.^{2}. Boundary of available 3D seismic data in red box. Locations of wells with acquired in relation to the seismic data shown in purple, all other wells in the area are shown in orange.

Appendix B: Measurements Locations and Calculated Variables

Table B1. Measured and calculated values of the meander morphology in 6 coeval Horizons spanning the geologic history of the channel. Measurements were taken 3 times at each location and averaged to reduce measurement error.

		Measured Variables							Calculated Variables			
Horizon	Data Point Location	Ls Stream Length	Lv Valley Length	r (ft) Meander Bend Radius	λ (ft) Meander Wavelength	1/2 λ (ft) Half Meander Wavelength	ω (ft) Channel Width	Mw (ft) Meander Width	K Sinuosity	C Curvature Ratio	L Length-Width Ratio	λ_{ratio} Wavelength Ratio
Sea Floor	A	8413	7757	873	3664	2105	361	1198	1.08457	2.41828	3.05843	0.57451
	B	10334	9659	814	2563	1320	346	731	1.06988	2.35260	3.50616	0.51502
	C	15170	13181	1437	7327	3228	483	2866	1.15090	2.97516	2.55652	0.44056
Horizon 6	A	6698	4991	858	3537	1492	441	2424	1.34202	1.94558	1.45916	0.42183
	B	6076	5085	819	2747	1098	474	2422	1.19489	1.72785	1.13419	0.39971
	C	5797	5474	729	3059	1724	659	1194	1.05901	1.10622	2.56198	0.56358
	D	7520	6262	764	2527	988	531	1563	1.20089	1.43879	1.61676	0.39098
	E	8685	4637	579	1701	812	711	2161	1.87298	0.81435	0.78714	0.47737
	F	4928	4056	642	1593	929	692	1620	1.21499	0.92775	0.98333	0.58318
	G	7418	5057	834	2339	1468	619	1841	1.46688	1.34733	1.27051	0.62762
	H	5095	4056	774	1428	788	690	1821	1.25616	1.12174	0.78418	0.55182
Horizon 5	A	10965	9390	1554	6190	3019	431	2934	1.16773	3.60557	2.10975	0.48772
	B	15568	14295	1778	7024	3917	686	3025	1.08905	2.59184	2.32198	0.55766
	C	23577	21354	1732	16741	7879	988	5205	1.10410	1.75304	3.21633	0.47064
	D	15397	14364	1941	15219	7703	870	4698	1.07192	2.23103	3.23946	0.50614
	E	14898	13792	1743	8648	4299	1169	3948	1.08019	1.49102	2.19048	0.49711
	F	11336	11590	2365	12056	5099	1197	3166	0.97808	1.97577	3.80796	0.42294
Horizon 4	A	1773	1552	122	516	224	156	331	1.14240	0.78205	1.55891	0.43411
	B	2506	1568	213	845	348	138	481	1.59821	1.54348	1.75676	0.41183
	C	1935	1671	239	960	560	207	531	1.15799	1.15459	1.80791	0.58333
	D	5038	3434	624	2288	989	488	1727	1.46709	1.27869	1.32484	0.43226
	E	4712	3077	540	1428	647	452	1437	1.53136	1.19469	0.99374	0.45308
	F	6601	5593	971	4170	2056	720	1198	1.18023	1.34861	3.48080	0.49305
	G	7503	4258	549	1739	855	619	1789	1.76209	0.88691	0.97205	0.49166
	H	4464	3892	661	2326	1124	462	1711	1.14697	1.43074	1.35944	0.48323
Horizon 3	A	3940	2493	272	1497	701	162	802	1.58043	1.67901	1.86658	0.46827
	B	4369	2796	333	1274	741	237	1129	1.56259	1.40506	1.12843	0.58163
	C	5391	4685	498	2988	1401	445	1697	1.15069	1.11910	1.76075	0.46888
	D	4897	3797	620	2441	1009	497	1312	1.28970	1.24748	1.86052	0.41336
	E	4065	3422	646	2036	1225	332	989	1.18790	1.94578	2.05865	0.60167
	F	3239	2502	485	2003	974	317	1289	1.29456	1.52997	1.55392	0.48627
Horizon 2	A	5301	4830	498	2426	1124	403	979	1.09752	1.23573	2.47804	0.46331
	B	3629	2959	381	1424	652	165	855	1.22643	2.30909	1.66550	0.45787
	C	5807	3950	656	2227	1044	578	1510	1.47013	1.13495	1.47483	0.46879
	D	4482	3791	651	2573	1199	599	1610	1.18227	1.08681	1.59814	0.46599
	E	3672	2736	548	1801	1148	403	1249	1.34211	1.35980	1.44195	0.63742
	F	6213	4427	874	3316	1730	748	2588	1.40343	1.16845	1.28130	0.52171
	G	3304	2747	527	1931	812	707	2019	1.20277	0.74540	0.95641	0.42051
Horizon 1	A	6517	6371	1166	11740	3789	738	2531	1.02292	1.57995	4.63848	0.32274
	B	7823	7526	974	11146	6770	808	2194	1.03946	1.20545	5.08022	0.60739
	C	4061	3430	446	2163	1081	313	1056	1.18397	1.42492	2.04830	0.49977
	D	6924	4194	527	1741	908	355	1412	1.65093	1.48451	1.23300	0.52154
	E	5431	4094	930	2364	1465	298	1482	1.32658	3.12081	1.59514	0.61971
	F	5210	3406	538	2331	1083	283	1531	1.52965	1.90106	1.52253	0.46461

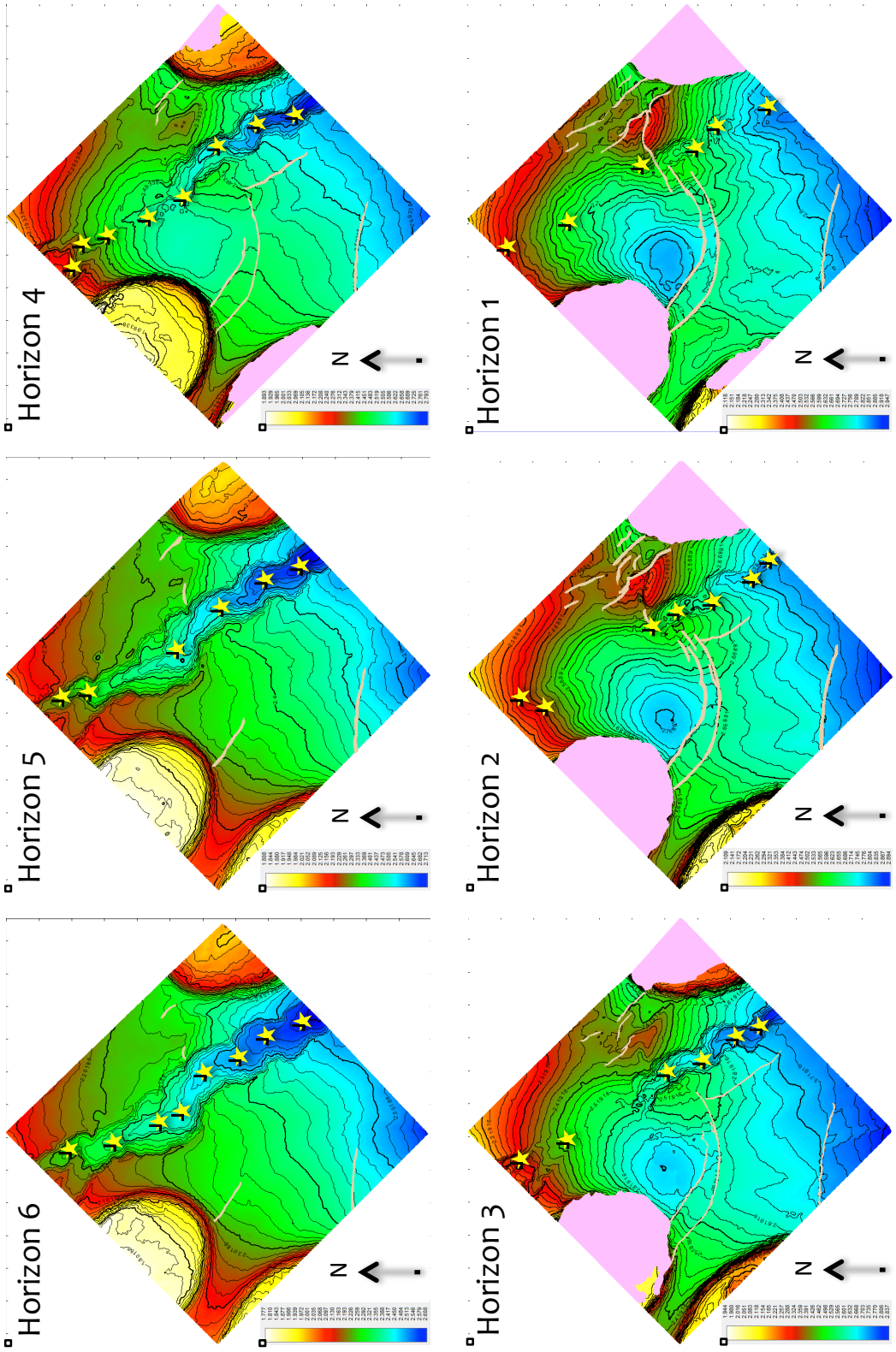

Figure B1. Contour maps of horizon slices utilized in this study. Gold starts represent locations of collected measurements.

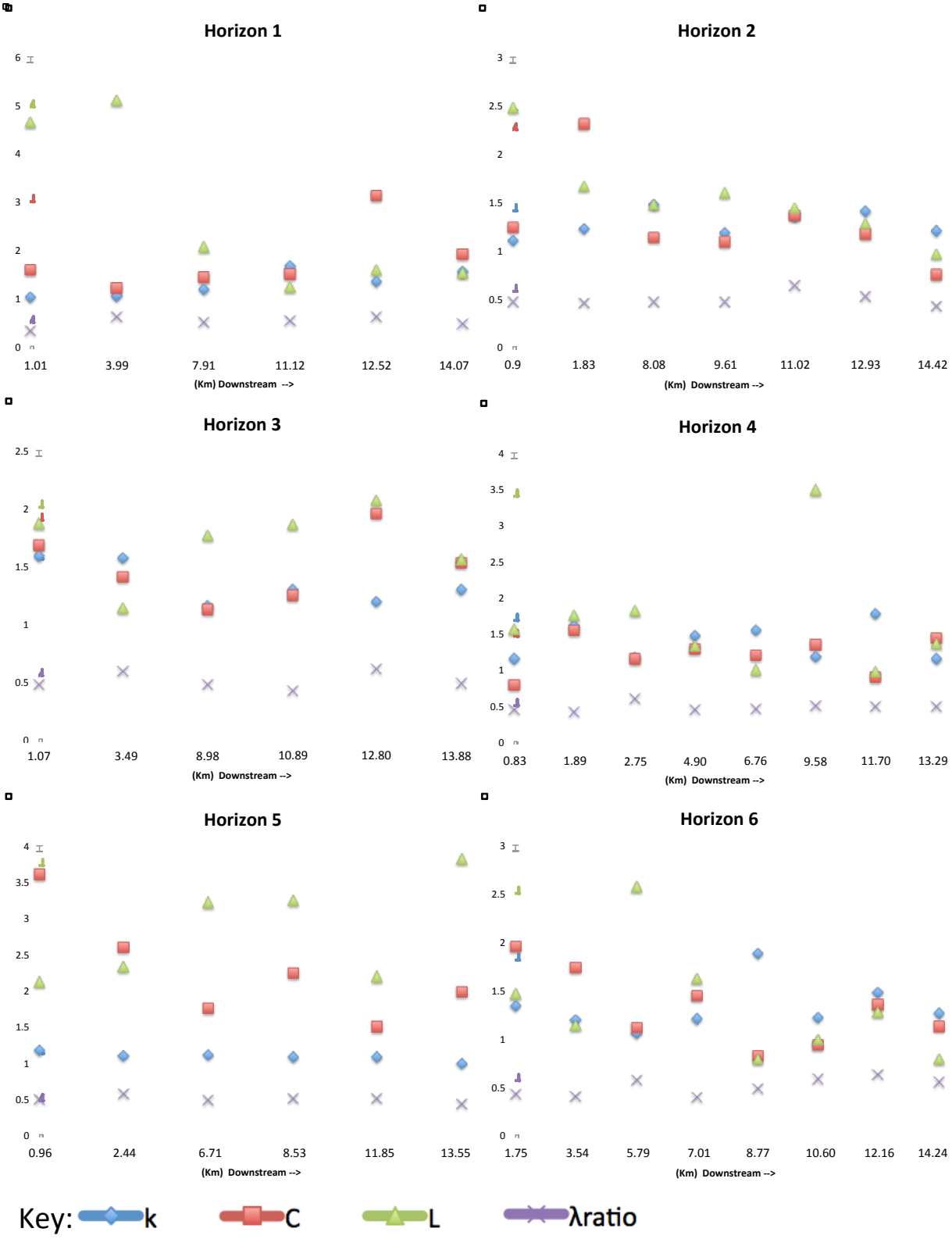

Figure B2. Downstream Relationship of Calculated Variables.

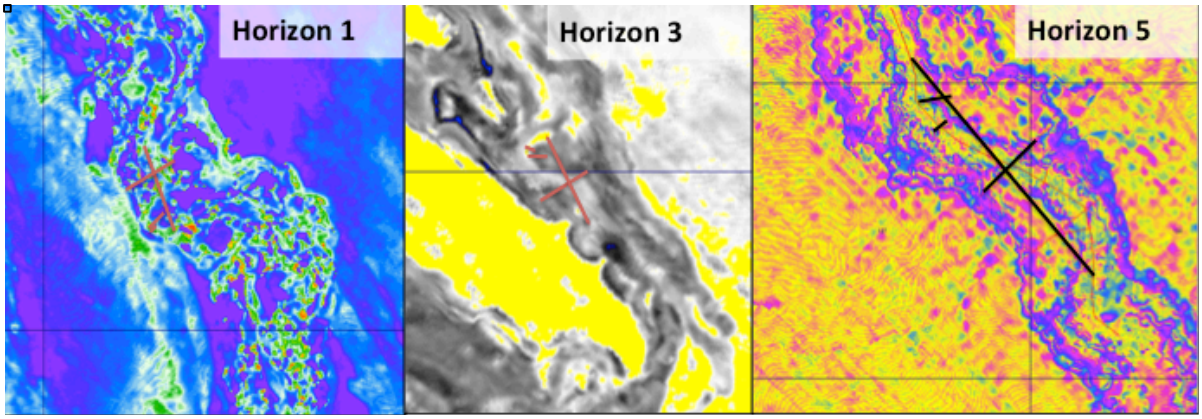

Figure B3. Example of measurement collection method. Figure shows horizon 1, 2 and 3 from left to right.

Appendix C: Seismic Attributes

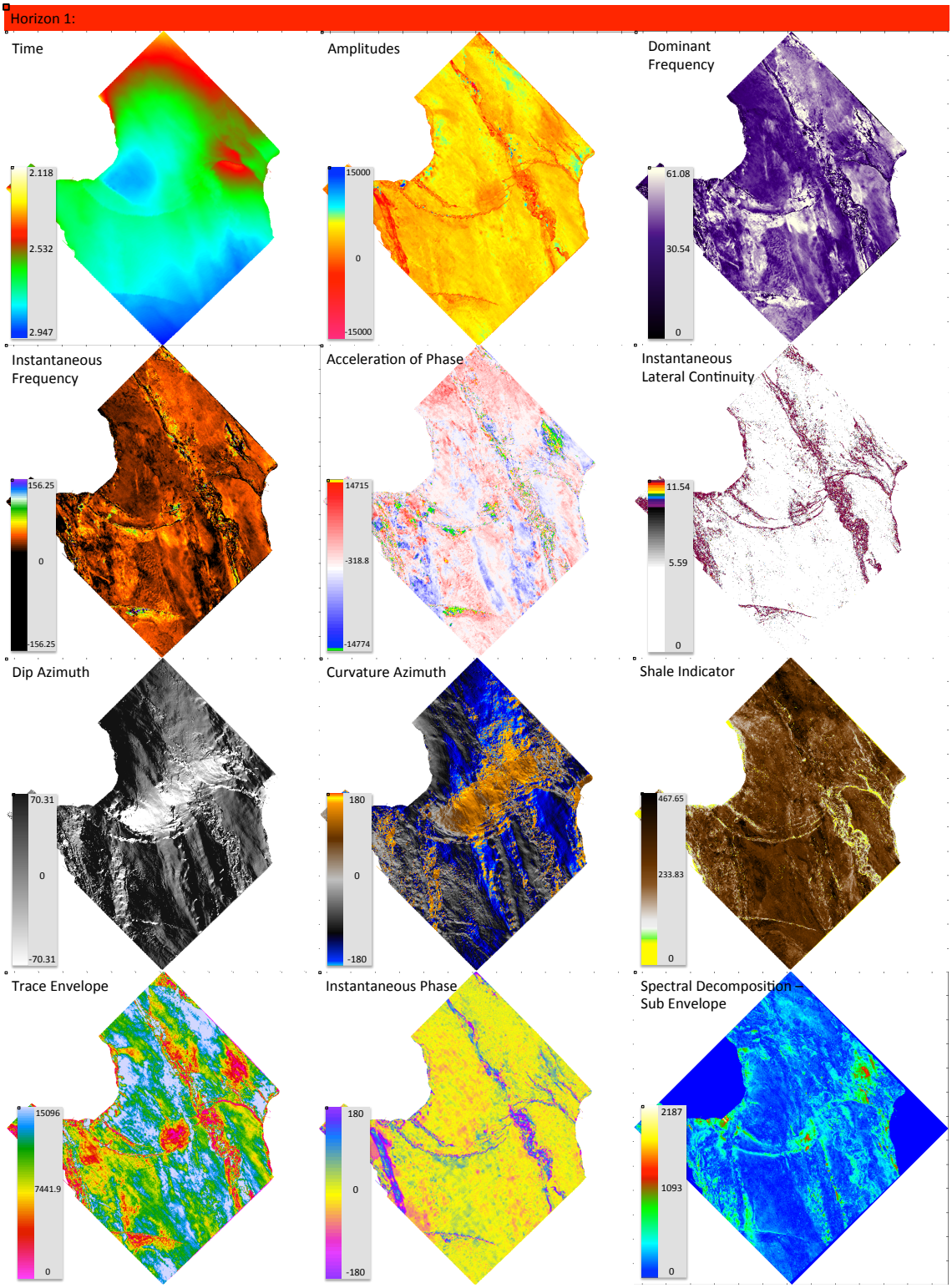

Figure C1. Seismic attributes performed on horizon 1. Associated color scales are shown in the bottom left corner of the box for each attribute.

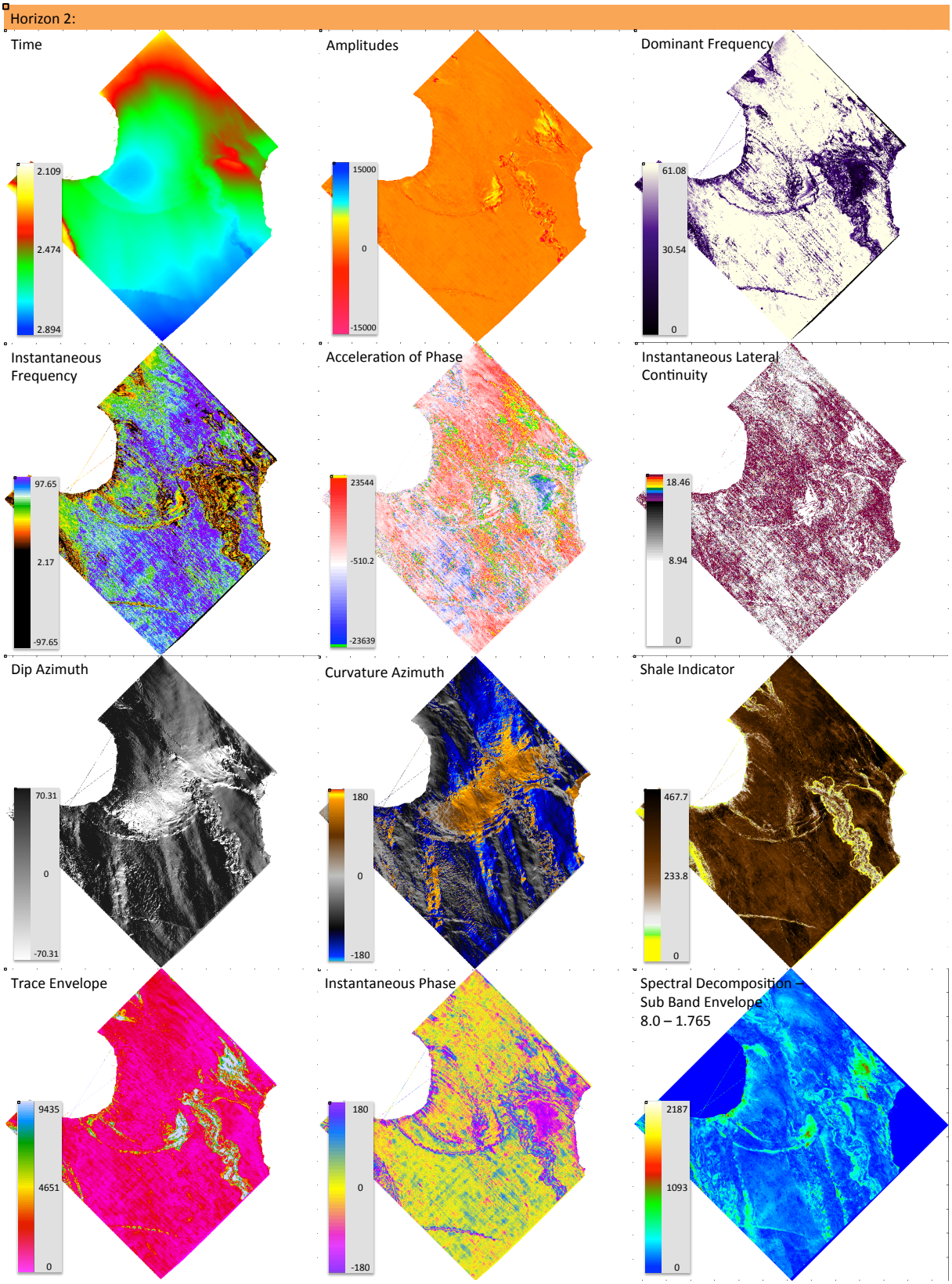

Figure C2. Seismic attributes performed on horizon 2. Associated color scales are shown in the bottom left corner of the box for each attribute.

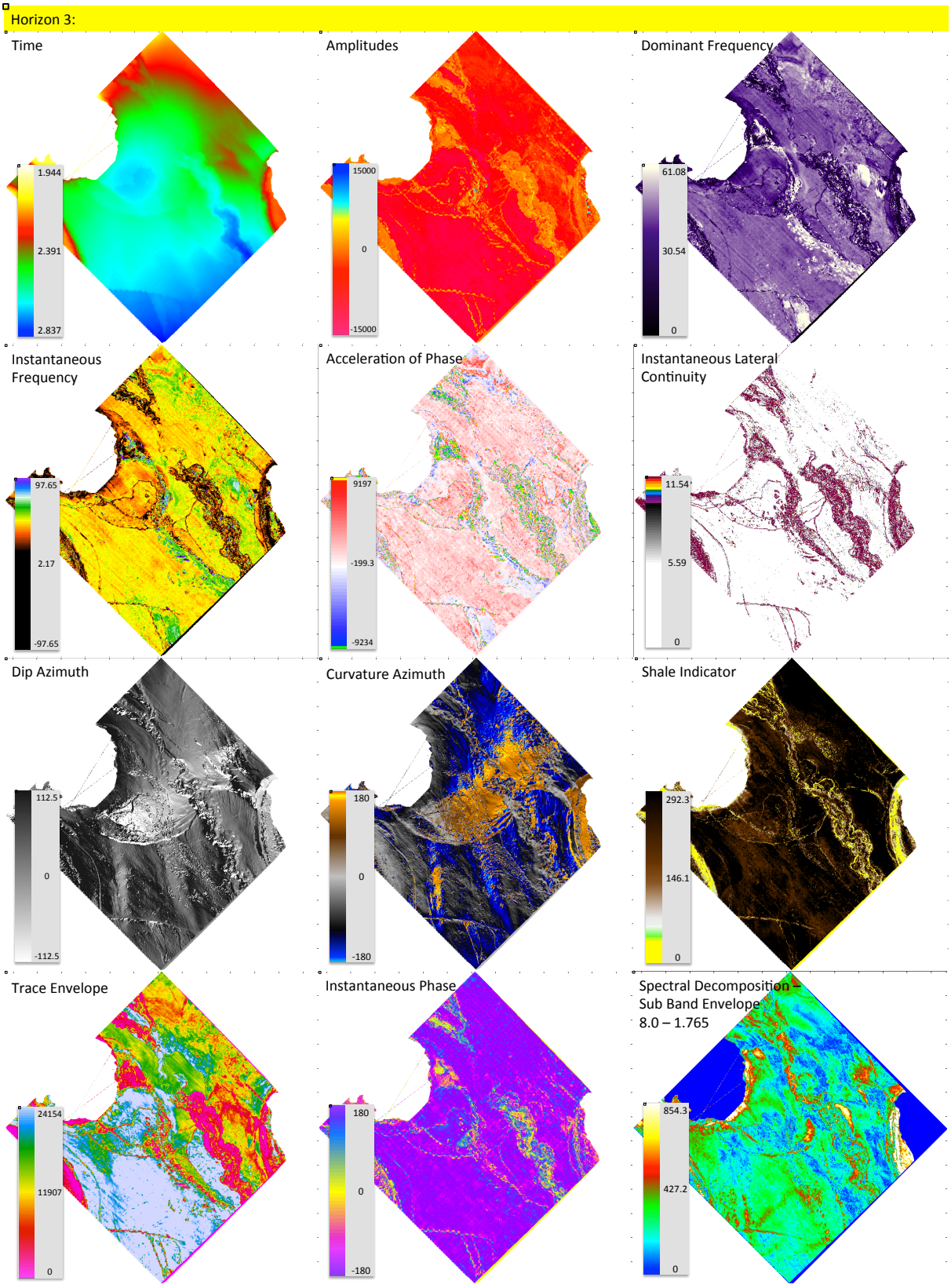

Figure C3. Seismic attributes performed on horizon 3. Associated color scales are shown in the bottom left corner of the box for each attribute.

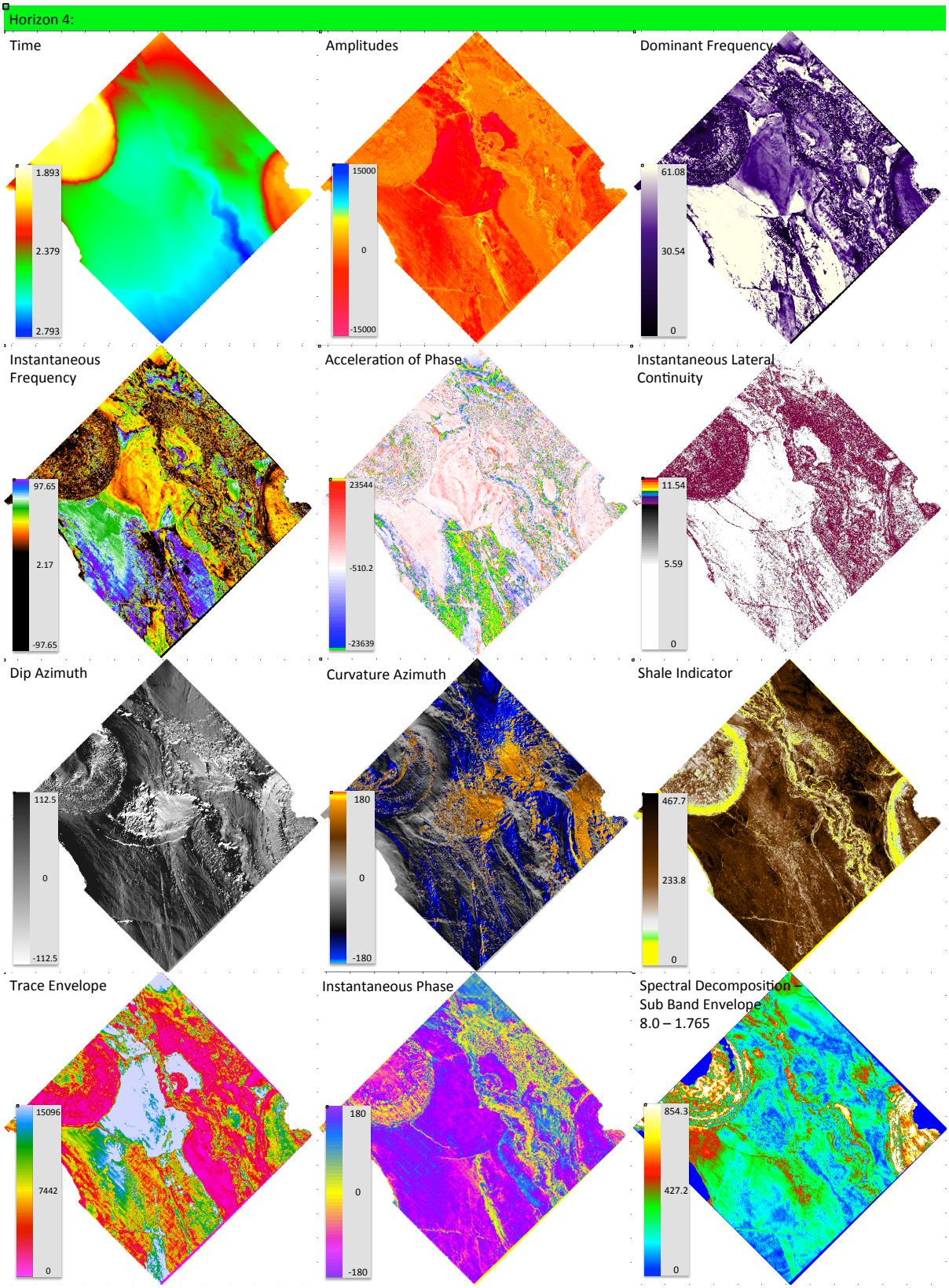

Figure C4. Seismic attributes performed on horizon 4. Associated color scales are shown in the bottom left corner of the box for each attribute.

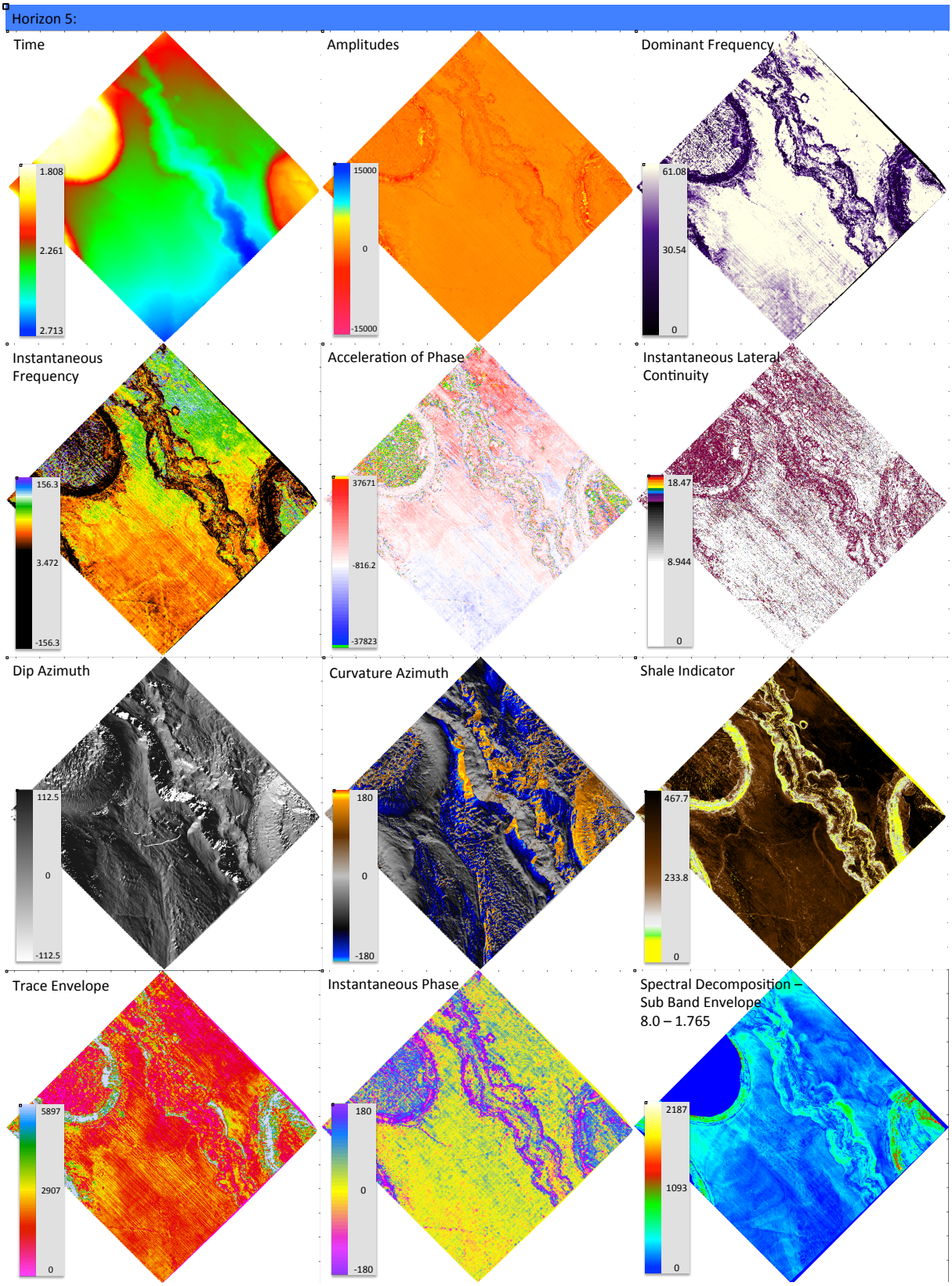

Figure C5. Seismic attributes performed on horizon 5. Associated color scales are shown in the bottom left corner of the box for each attribute.

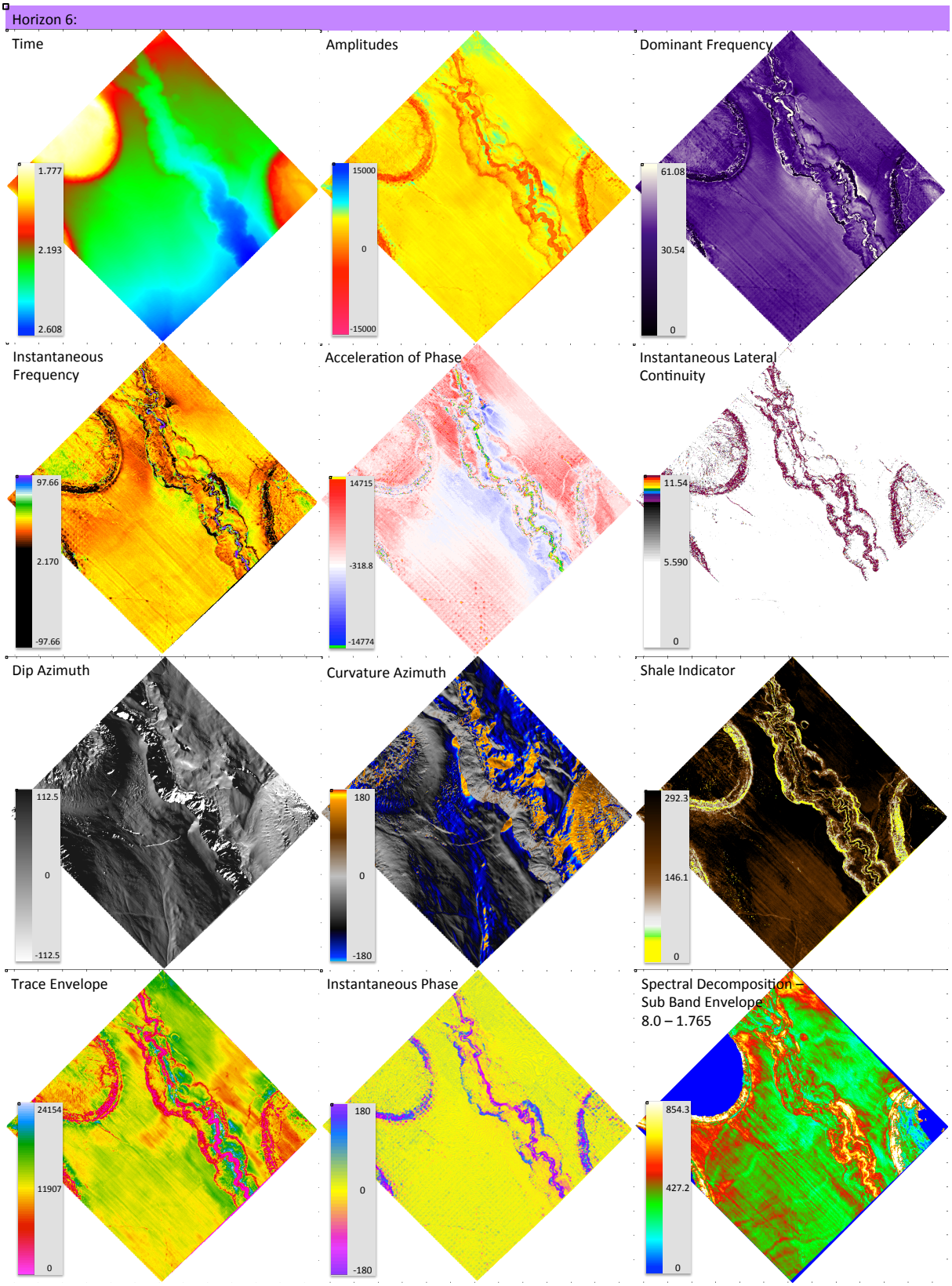

Figure C6. Seismic attributes performed on horizon 6. Associated color scales are shown in the bottom left corner of the box for each attribute.

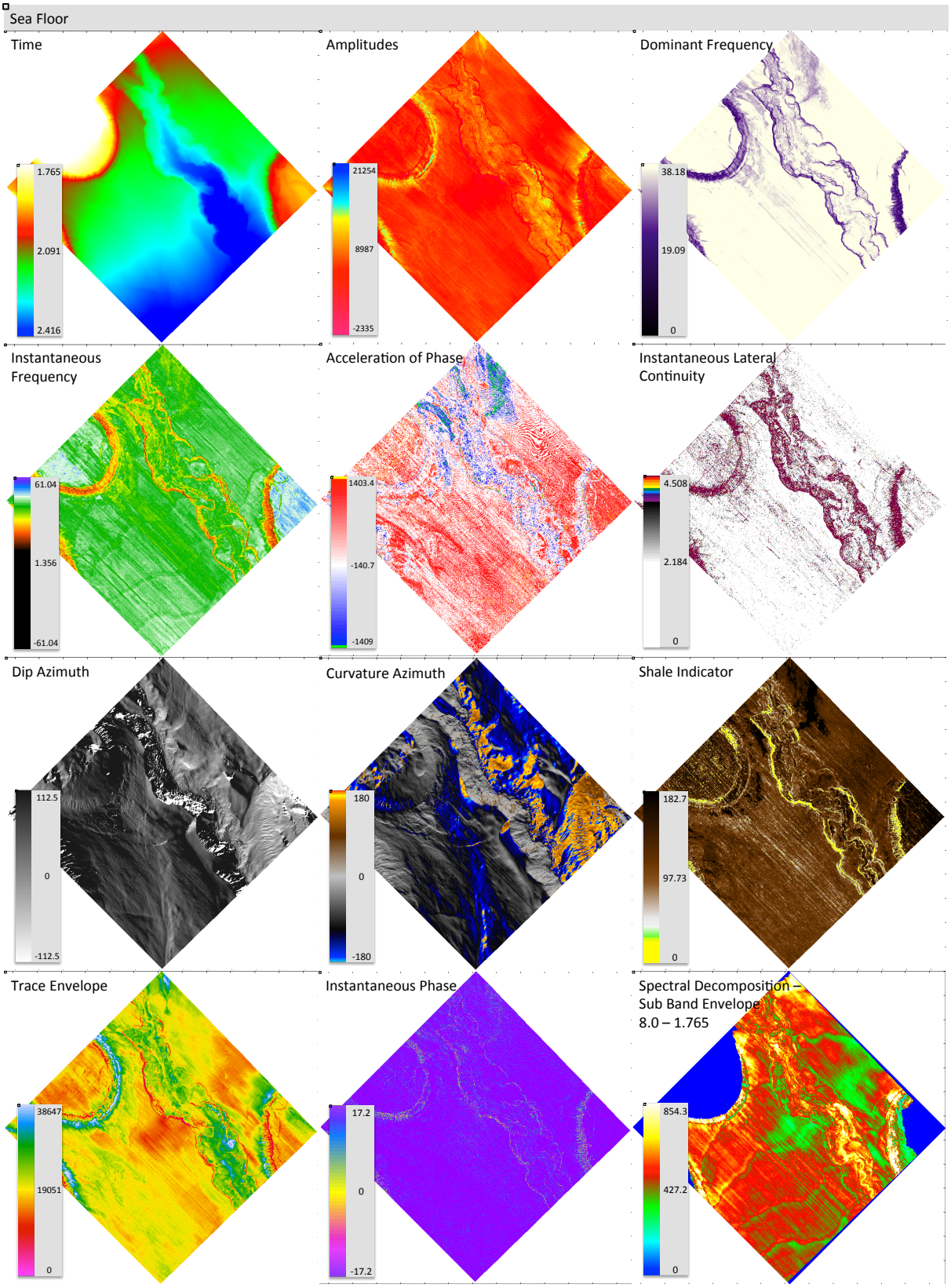

Figure C7. Seismic attributes performed on the sea floor. Associated color scales are shown in the bottom left corner of the box for each attribute.

Appendix D: Graphs of Meander Properties

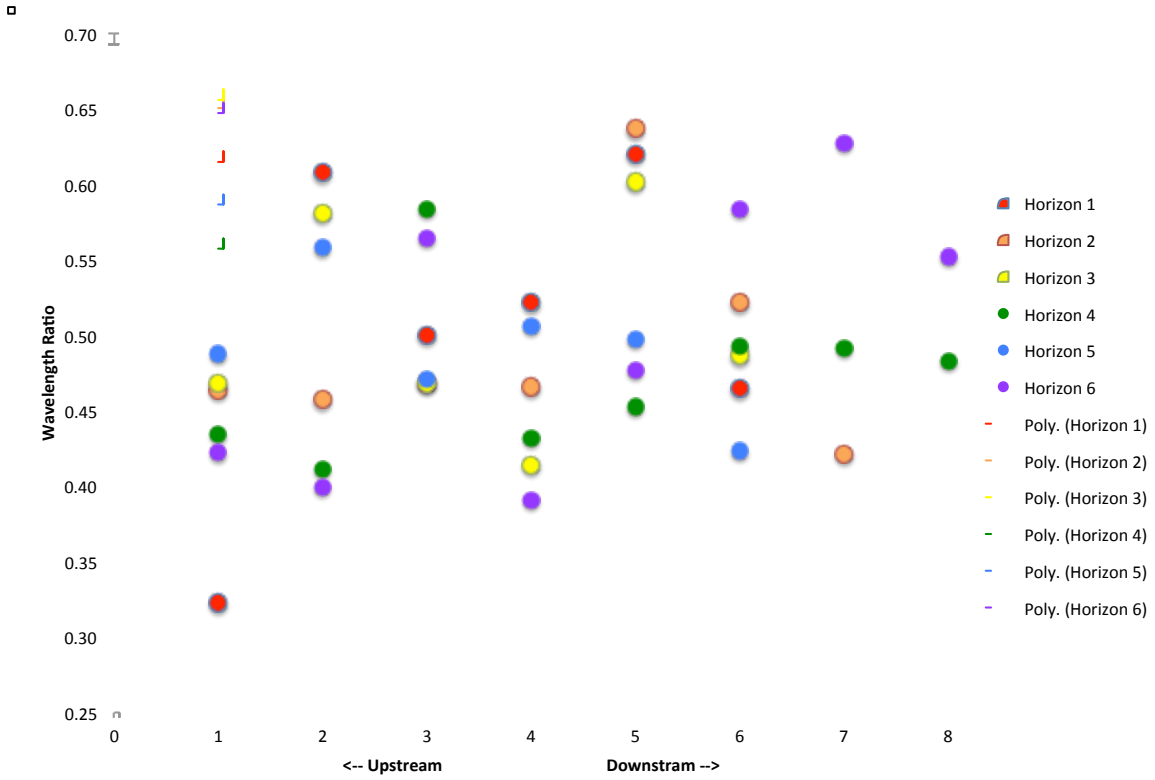

Figure D1. Downstream changes in wavelength ratio. Polynomial equations for each horizon are shown. Horizons 1, 2 and 3 depict a similar pattern. Horizon 4 and 6 show a similar pattern. Horizon 5 does not appear to match either pattern.

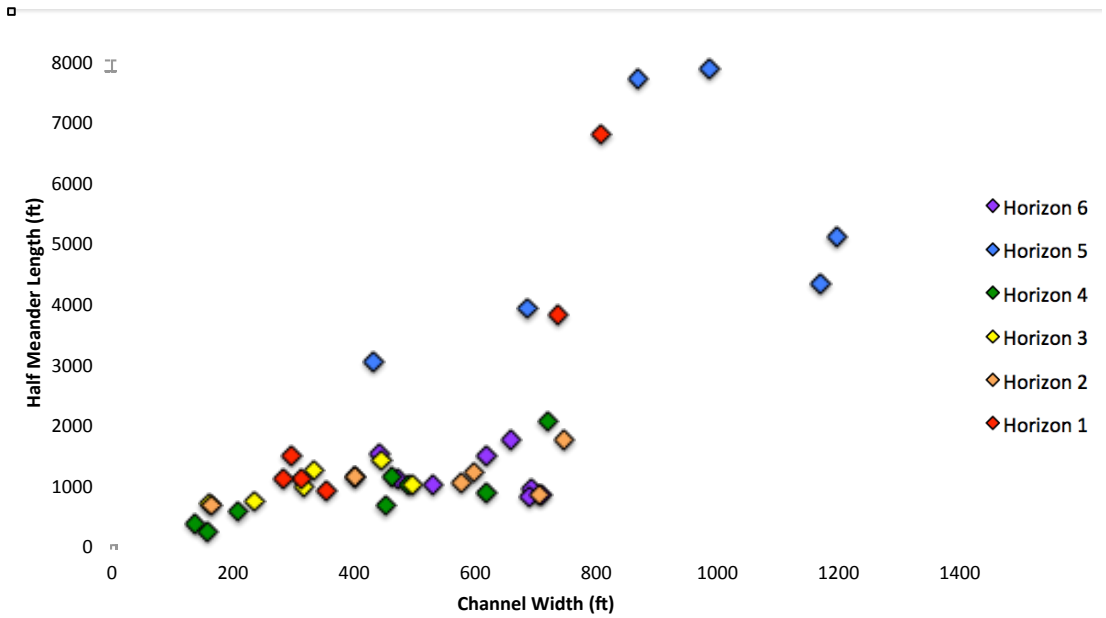

Figure D2. Channel width vs. half meander length.

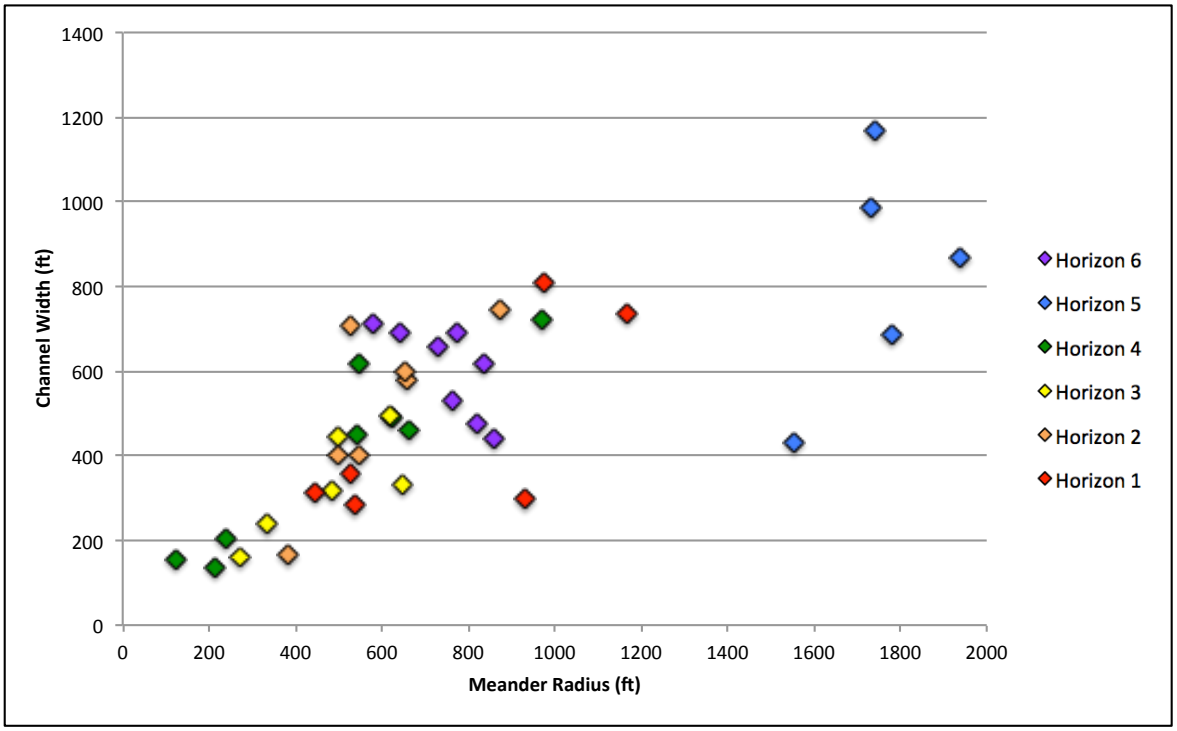

Figure D3. Meander radius vs. channel width.

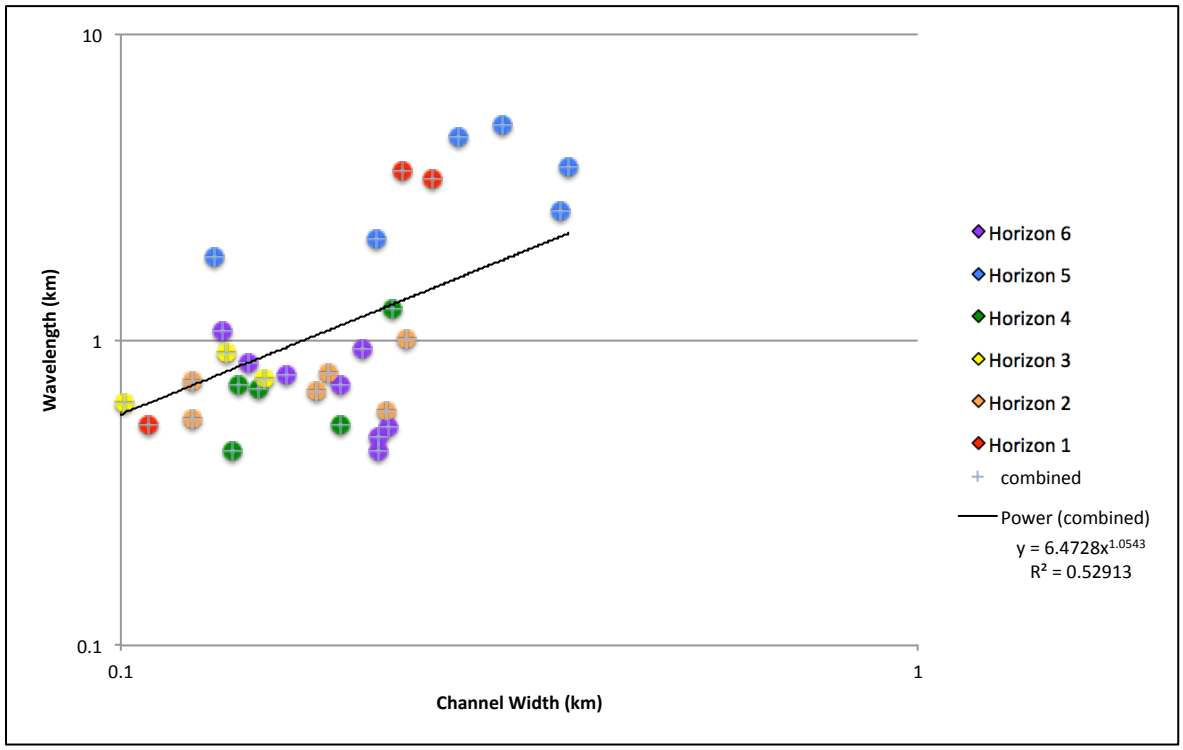

Figure D4. Wavelength vs. channel width presented on a log-log scale.

Vita

Rachel Carter was born in St. Louis, Mo in 1987. She moved to Kansas City, KS in 1989 where she completed the majority of her public school education, graduating from Blue Valley North West High School in 2006. Rachel attended multiple colleges, receiving an Associate of Arts degree from Johnson County Community College in 2010. It was at the community college that Rachel happened upon Geology and the Earth Sciences, an instant passion developed. She moved to the University of New Orleans in 2011 in order to pursue this newfound thirst for knowledge about how the Earth worked. After a summer internship with Murphy Oil in 2012 Rachel decided that the science of petroleum geology was her future. Rachel graduated with a Bachelor's in Earth Science from the University of New Orleans in 2013, and began her graduate career the following semester.